Quaternary Science Reviews 299 (2023) 107854

Contents lists available at ScienceDirect

Quaternary Science Reviews

journal homepage: www.elsevier.com/locate/quascirev

Storm chasing: Tracking Holocene storminess in southern Sweden using mineral proxies from inland and coastal peat bogs

Malin E. Kylander [a, b, *], Antonio Martínez-Cortizas [b, c], Jenny K. Sjöström [a, b], Jenny Gåling [a, b], Richard Gyllencreutz [a, b], Richard Bindler [d], Helena Alexanderson [e, f], Frederik Schenk [a, b], Benedict T.I. Reinardy [g], Benjamin M.P. Chandler [h], Kerry Gallagher [i]

[a] Department of Geological Sciences, Stockholm University, Stockholm, Sweden
[b] Bolin Centre for Climate Research, Stockholm University, Stockholm, Sweden
[c] CRETUS, EcoPast (GI-1553), Universidade de Santiago de Compostela, Santiago de Compostela, Spain
[d] Department of Ecology and Environmental Science, Umeå University, Umeå, Sweden
[e] Department of Geology, Lund University, Lund, Sweden
[f] Department of Geosciences, The Arctic University of Norway, Tromsø, Norway
[g] Department of Sustainable Development, Environmental Science and Engineering (SEED), KTH the Royal Institute of Technology, Stockholm, Sweden
[h] School of Geography, University of Nottingham, Nottingham, UK
[i] University of Rennes, CNRS, Géosciences Rennes, Rennes, France

ARTICLE INFO

Article history:
Received 19 July 2022
Received in revised form
1 November 2022
Accepted 2 November 2022
Available online 25 November 2022

Keywords:
Storms
Holocene
Peat
Paleoclimate
Scandinavia
Mineralogy
Inorganic geochemistry

ABSTRACT

Severe extratropical winter storms are a recurrent feature of the European climate and cause widespread socioeconomic losses. Due to insufficient long-term data, it remains unclear whether storminess has shown a notable response to changes in external forcing over the past millennia, which impacts our ability to project future storminess in a changing climate. Reconstructing past storm variability is essential to improving our understanding of storms on these longer, missing timescales. Peat sequences from coastal ombrotrophic bogs are increasingly used for this purpose, where greater quantities of coarser grained beach sand are deposited by strong winds during storm events. Moving inland however, storm intensity decreases, as does sand availability, muting potential paleostorm signals in bogs. We circumvent these issues by taking the innovative approach of using mid-infrared (MIR) spectral data, supported by elemental information, from the inorganic fraction of Store Mosse Dune South (SMDS), a 5000-year-old sequence from a large peatland located in southern Sweden. We infer past changes in mineral composition and thereby, the grain size of the deposited material. The record is dominated by quartz, whose coarse nature was confirmed through analyses of potential local source sediments. This was supported by further mineralogical and elemental proxies of atmospheric input. Comparison of SMDS with within-bog and regionally relevant records showed that there is a difference in proxy and site response to what should be similar timing in shifts in storminess over the ~100 km transect considered. We suggest the construction of *regional storm stacks*, built here by applying changepoint modelling to four transect sites jointly. This modelling approach has the effect of reinforcing signals in common while reducing the influence of random noise. The resulting Southern Sweden-Storm Stack dates stormier periods to 4495–4290, 3880–3790, 2885–2855, 2300–2005, 1175–1065 and 715-425 cal yr BP. By comparing with a newly constructed Western Scotland-Storm Stack and proximal dune records, we argue that regional storm stacks allow us to better compare past storminess over wider areas, gauge storm track movements and by extension, increase our understanding of the drivers of storminess on centennial to millennial timescales.

1. Introduction

Observations from Europe covering the last ~120 years have shown a strong increase in windstorms towards the end of the 20th

* Corresponding author. Department of Geological Sciences, Stockholm University, Stockholm, Sweden.
E-mail address: malin.kylander@geo.su.se (M.E. Kylander).

https://doi.org/10.1016/j.quascirev.2022.107854

century (e.g., Feser et al., 2014; Rutgersson et al., 2014), while relatively calm conditions have prevailed during the 21st century (Rutgersson et al., 2022; Stendel et al., 2016). A review dating back to the 18th century in the region showed no consistent long-term trends (Feser et al., 2014) and hints at the dominance of multi-decadal variability, with no information on centennial to millennial timescales. The most recent IPCC report gives a spatially heterogenous future picture for Europe: with the exception of the British Isles, Denmark and southern Sweden, winter *storminess* (a term encompassing both storm frequency and intensity) is expected to decrease. There is however, low agreement amongst models and as a result, "low confidence in projected regional changes" (IPCC, 2021). Part of this uncertainty stems from a poor understanding of changes occurring on longer, pre-instrumental and pre-anthropogenic timescales. One way to fill this knowledge gap is through the reconstruction of past storminess using paleo-environmental archives, which give us a window into the undisturbed climate of the past.

Over the last two decades, it has become increasingly common to use peat sequences from coastal areas to gain a temporally continuous picture of changes in paleostorminess (e.g., Björck and Clemmensen, 2004; Orme et al., 2016; Kylander et al., 2020). Ombrotrophic bogs are likened to "green glaciers" where they are fed through wet and dry deposition solely, and therefore reflect atmospheric processes. Such deposits are common in the wetter and colder reaches of mid- and high-latitude Europe, and records often stretch back to the mid- and even early-Holocene (Loisel et al., 2014). Peat has the advantage that it is easily dated and can be sub-sampled at near-decadal resolution. Peat paleostorm records were first introduced by Björck and Clemmensen (2004) where they developed the aeolian sand index (ASI), based on the accumulation of mineral grains between 200 and 350 μm and >350 μm. This was partnered with measurements of peat ash residue after loss on ignition (LOI), which represents the amount of mineral material deposited on the bog. The underlying assumption is that greater quantities and coarser material from coastal beaches and dunes is exported inland by stronger winds – like those during storms. Since this early work, storminess proxies in peat paleorecords have been continuously developing. This has included ASI-inspired proxies such as sand weight (fractions above >120 μm) and sand fluxes (Orme et al., 2016), sand mass accumulation rates (MAR; Sjögren, 2009), as well as total grain size analyses (Kylander et al., 2020). Halogens have been used as indicators of increased sea salt spray during storms (Orme et al., 2015; Stewart et al., 2017), although this has not shown to be universally applicable (Kylander et al., 2020). Multi-element approaches have also revealed changes in the source, grain size and magnitude of minerals being deposited on bogs through, for example, Si/Al ratios and elemental MAR (Kylander et al., 2020; Martinez-Cortizas et al., 2020; Sjöström et al., 2022).

Storms crossing the North Atlantic generally follow a common storm track as they move eastwards and are at their strongest as they make landfall on the western shores of Europe (Feser et al., 2014). Therefore, it is natural that many paleostorm reconstructions are from coastal areas. Indeed, this is where we expect signals to be at their strongest, which translates into more obvious changes in paleostorm proxies. Storms do not, however, stop at coastal areas, and they can have a devastating impact on the landscape as they move inland. When the windstorm Gudrun hit southern Sweden in January 2005, wind speeds of 30–35 m s^{-1} (>100–126 km h^{-1}) were measured in the central province of Småland, with peak gusts of 42 m s^{-1} (151 km h^{-1}) at Hanö. In the county of Kronoberg alone, storm winds felled the equivalent of six years of normal timber harvest and caused power outages, disruption to transport systems and even death (Skogsstyrelsen, 2017; SMHI, 2015).

In comparison to peat paleostorm reconstructions from coastal sites, inland sites are faced with two main methodological challenges. First, there are usually no comparatively large sand sources in the landscape, and if there are, they are often vegetated. Second, wind speeds often taper as storms move inland, muting the proxy signal. As such, more refined methods for identifying changes in the quantity and grain size of the archived inorganic material are needed. Direct measurement/identification of the inorganic fraction in peats is complicated by its highly organic matrix (often >95%). Removal of the organic fraction using combustion methods can impact mineral identification and grain size analyses through collapsing of clays and destroying of aggregates, respectively (Sjöström et al., 2019). We find increasing evidence that new minerals are generated during combustion, which complicates both mineralogical identification and grain size analyses. On the other hand, acid-based methods have been found to be ineffective in removing such large amounts of resistant organic matter (Rudmin et al., 2018; Sjöström et al., 2019). Different analytical approaches also have inherent characteristics that must be considered when attempting to establish the mineral content of a sample. For example, although X-ray diffraction (XRD) is a well-established tool for mineral identification and quantification, it is restricted to crystalline phases, which requires that organic matter (OM, >3–5 wt%) is removed, and minor mineral occurrences (<1%) may be overlooked due to peak overlap (Sjöström et al., 2019; Rudmin et al., 2018). Multi-element analyses have also been used to infer mineral composition, and thereby grain size, of peats (Kylander et al., 2016; Sjöström et al., 2020, 2022), but this should be combined with supporting analyses in order to anchor mineral inferences (e.g., XRD, SEM-EDS; Sjöström et al., 2022). More recently, attenuated total reflectance Fourier-transform infrared spectroscopy (FTIR-ATR), a quick and non-destructive analysis, has been introduced as a method for establishing the mineral composition of the inorganic fraction in peats. Martínez-Cortizas et al. (2021b) used IR spectra, processed with Principal Component Analysis (PCA), to extract changes in quartz, K-feldspar, mica and plagioclase over time from a minerogenic mire in northwestern Spain. These changes could then be linked to deforestation and consequent shifts in erosion and hydrology.

Store Mosse (in Swedish *the Great Bog*) is an extensive bog complex (~100 km^2) located in Småland, south-central Sweden (Fig. 1). It has been the subject of numerous studies, particularly in its southern reaches, where the deepest and oldest accumulations have been found (~9000 years recorded in ~6.5 m of peat; Kylander et al., 2018, 2016, 2013; Ryberg et al., 2022; Svensson, 1988). Store Mosse is unique in that it is not only bisected by a string of sand dunes, but also ringed by aeolian deposits and glaciofluvial sediments, providing abundant local sources of coarser-grained material. Studies from the southern portion of the bog based on the Store Mosse South-2008 sequence (SMS_{2008}) suggested the deposition of relatively coarse-grained local material between 5300 and 4370 cal yr BP (Kylander et al., 2016, 2018), perhaps as a consequence of the stormier conditions identified at 4900 and 4550 cal yr BP in southern Sweden (Björck and Clemmensen, 2004). We speculated that the within-bog dunes may be the source of this material. If this reasoning is correct, then sites closer to the dunes should present stronger signals of coarse-grained input.

We set out to test if this was the case with the additional aim of building an inland peat paleostorm record – the first of its kind. We exploit the presence of coarse-grained material within and surrounding Store Mosse. Specifically, we analyse a network of 30 sites in order to constrain the mineralogy of potential sources and

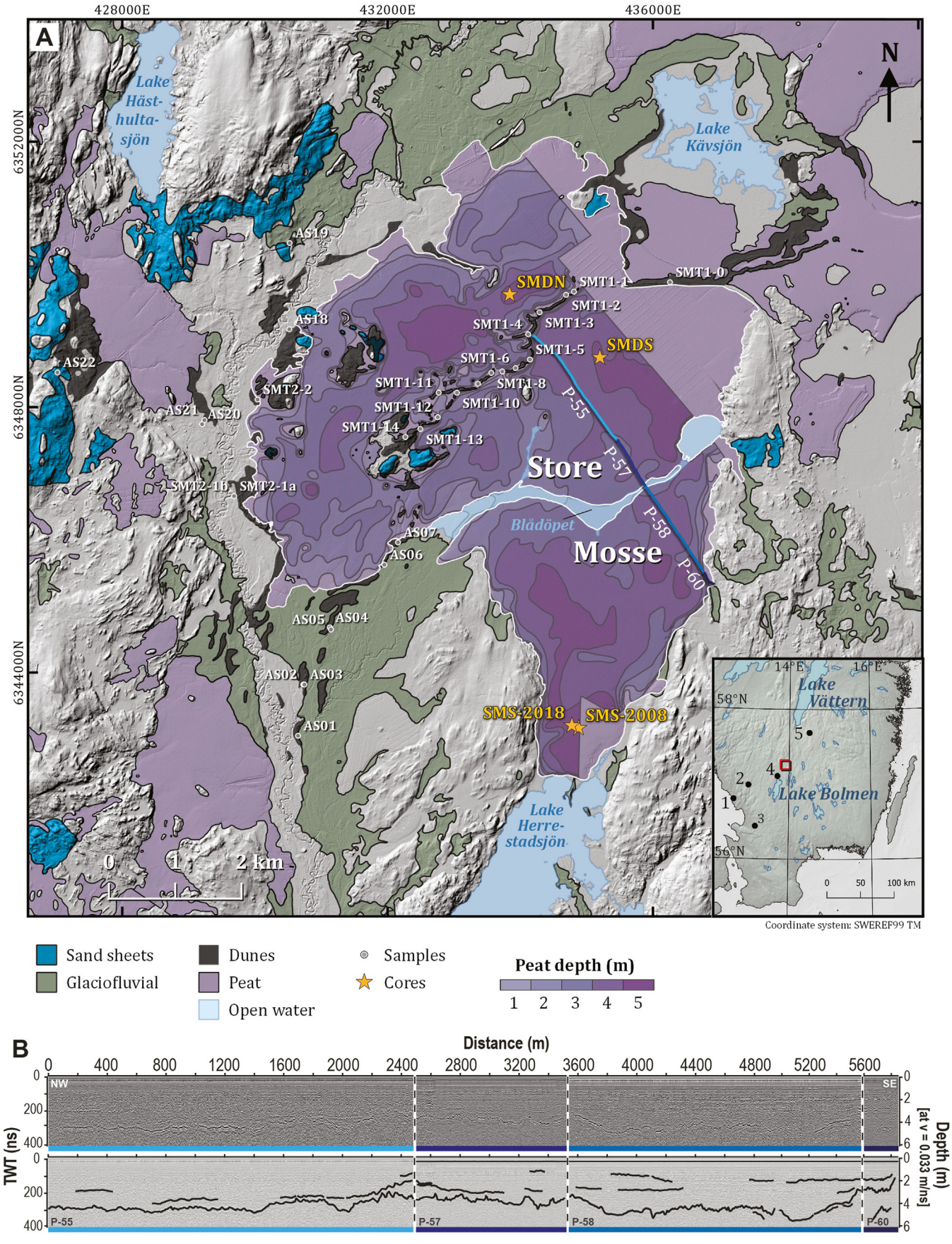
A
428000E
432000E
436000E
6352000N
6348000N
6344000N
N
Lake Häst-hulta-sjön
Lake Kävsjön
AS19
AS18
AS22
AS21
AS20
SMT2-2
SMT2-1b
SMT2-1a
AS07
AS06
AS05
AS04
AS02
AS03
AS01
SMDN
SMT1-1
SMT1-0
SMT1-2
SMT1-4
SMT1-3
SMT1-5
SMDS
SMT1-6
SMT1-11
SMT1-8
SMT1-12
SMT1-10
SMT1-14
SMT1-13
P-55
P-57
P-58
P-60
Store
Mosse
Bládöpet
SMS-2018
SMS-2008
Lake Herre-stadsjön
0 1 2 km
14°E
16°E
58°N
56°N
Lake Vättern
Lake Bolmen
1
2
3
4
5
0 50 100 km
Coordinate system: SWEREF99 TM
Sand sheets
Glaciofluvial
Dunes
Peat
Open water
Samples
Cores
Peat depth (m)
1 2 3 4 5
B
Distance (m)
0 400 800 1200 1600 2000 2400 2800 3200 3600 4000 4400 4800 5200 5600
NW
SE
TWT (ns)
Depth (m) [at v = 0.033 m/ns]
P-55
P-57
P-58
P-60

identify any grain size fractionation information relevant to a paleostorm reconstruction. This is used to inform the analysis and interpretation of a peat sequence collected ~1 km to the south of the Store Mosse dune system. We take the unique approach of using mid-infrared (MIR) spectral data, supported by elemental information, from the inorganic fraction of the peat to infer the mineral composition, and thereby, the grain size of the deposited material. This is used to reconstruct the occurrence of stormier periods with more windstorms. In this study, we define windstorms as events with higher wind speeds and little or no rain that are most likely tied to large-scale cyclonic storms. Locally high wind speeds due to convective storms, i.e., thunderstorms, are not expected to be captured through coarse-grained input because these are accompanied by heavy rain that would inhibit transport. The objectives of this study are to: (i) characterise the local potential source samples in terms of dominant mineralogy and any links to grain size; (ii) establish changes in the mineral composition and, therefore, grain size, over time in the peat sequence; and (iii) evaluate the new dune-proximal peat record through comparison with SMS_{2008} (~5 km to the south) and other regionally relevant records. Our results show that there are differences in the paleostorm signals captured by different proxies within the same sequence, at the same site as well as across a wider transect of regional sites (~100 km). (iv) We present a way to address this issue and argue for the construction of *regional storm stacks* that allow for the tracing of storm track movements over time. The developments presented here have the potential to increase the spatial coverage of paleostorm records to inland areas and improve how we compare these records across wider geographic scales and thereby, increase our knowledge of Holocene storm dynamics.

2. Materials and methods

2.1. Study area

As stated previously, Store Mosse is located in Småland in south-central Sweden (Fig. 1). The development of the present-day landscape started with the retreat of the Scandinavian ice sheet ~14 ka BP (Lundqvist and Wohlfarth, 2000). In its wake a large ice-dammed lake formed, the Ancient Lake Bolmen. With isostatic uplift this lake was drained to the southwest leaving a low-lying, exposed lake bottom. This provided an appropriate habitat for the accumulation of peat, which started at the southern end of the bog-complex at ~9 ka (Ryberg et al., 2022). A recently uncovered map with 2771 peat depth measurements made in 1912 (Eller and Brenner, 1912) shows that the bog complex at Store Mosse is actually composed of several sub-basins with the larger, southernmost basin separated from the rest of the complex by a small stream/wetter area called Blådöpet (peat depths shown in Fig. 1). There are abundant glacial sediments in the area and aeolian reworking resulted in the emplacement of a string of dunes across the Store Mosse basin at ~8 to 6 ka (Bjermo, 2019). The present bog surface is dominated by *Sphagnum* mosses with many areas co-dominated by *Eriphorum vaginatum* L., *Tricophorum cespistosum* L. and *Rhynchospora alba* L., but also by *Calluna vulgaris* (L.) Hull, *Vaccinium oxycoccos* L. and *Erica tetralis* L. *Drosera* spp and lichens (mostly *Cladonia* spp) also occur extensively. Store Mosse sits in the Eastern Segment of the Sveconorwegian Orogen (1.7 Ga). The local lithology is comprised of various combinations of granite, granodiorite, syenitoid, quartz monzodiorite and their metamorphic equivalents, with the former being common to most units (SGU, 2022a).

Today the climate is maritime with relatively cool summers and mild winters. The annual average temperature is 5.5 °C and the average precipitation is 800 mm yr^{-1} (SMHI, 2009). Wind speed data from the nearest weather station at Hagshult, measured three times daily from 1943 to 2022 CE, gives an average wind speed of 2.7 ± 2.0 m s^{-1}. Wind strengths of 6 or higher on the Beaufort scale (11–14 m s^{-1}), indicating windstorm events, make up <0.1% of the measurements over this period. The majority of these events occurred during the winter months of January, February and March (SMHI, 2022). The area is under the direct influence of cyclones mostly coming in from the southwest across the North Sea, Denmark and the west coast of Sweden including severe storms like Gudrun in January 2005 (SMHI, 2005). While there are no long-term changes in severe storminess since late the 18th century, different storm indices indicate decadal clusters of unusually severe storms at least once per century (Bärring and Fortuniak, 2009; Schenk and Zorita, 2012; Rutgersson et al., 2015).

2.2. Sampling

In November 2014 and September 2018 local source samples, mostly aeolian in origin, were collected in and around Store Mosse (Fig. 1, Table 1). The samples come from an east-west transect along the dunes in the bog (SMT1 samples) as well as areas to the northwest and southwest of the bog (SMT2 and AS samples). For each site/deposit, a few grams of sample were collected by digging to below the active vegetation zone (20–30 cm depth).

Based on the depth map of Store Mosse, the northeastern corner of the central bog complex has accumulated material up to ~6 m thick (Eller and Brenner, 1912, Fig. 1). In November 2018 we attempted to sample this deeper accumulation, staying away from the peat cuttings in the northeast corner while remaining as close to the dunes as possible. The Store Mosse Dune South (SMDS) sequence (57°16′37.70″N, 13°55′30.86″E) was collected using a 1 m long Russian corer (diameter 10 cm). Six 1 m sections with 25 cm overlap were taken in two adjacent parallel holes to a depth of 450 cm. Cores were kept in a cold room until sub-sampling.

2.3. Ground-penetrating radar surveying

To examine the stratigraphy of Store Mosse, we undertook common-offset ground-penetrating radar (GPR) surveys. The GPR profiles were collected using a MALÅ ProEx system and an unshielded Rough Terrain Antenna (RTA) with a nominal central frequency of 100 MHz. The geographical location and elevation of the GPR data were collected simultaneously using a backpack-mounted GNSS receiver (Hemisphere A101). The GNSS receiver recorded GPS positions every 1 s. Full details of GPR corrections and processing are given in the Supplementary Data (SD Fig. 1) but follows the approach of Watts et al. (2022) assuming a wave speed typical for energy propagating through peat (e.g., Reynolds, 2011).

Fig. 1. (A) Overview map of Store Mosse and surrounding areas. The map is based on the extent of peat, aeolian sand sheets, dunes and glacifluvial material as excerpts from the Swedish Quaternary map "Jordartskartan 25,000–100 000" (© Geological survey of Sweden; SGU, 2022b), a 2-m resolution digital elevation model "GSD-Höjddata grid 2+" (© Lantmäteriet) and the peat thickness map by Eller and Brenner (1912). All thematic areas on the map are semi-transparent to show underlying hill-shaded topography, which is relatively flat in the areas of the shown sediment types. Store Mosse is located 163–168 m asl, and the map area elevation spans ~150–300 m asl. Locations for source samples and peat sequences are marked with circles and stars, respectively. Inset are the locations of Store Mosse (red square) and the comparison sites Undarsmosse (1), Davidsmosse (2), Hyltemosse (3), Draftinge mosse (4) and Lake Avegöl (5) (see text for references). (B, upper panel) Composite GPR profile (including profiles 55, 57, 58 and 60); (B, lower panel) interpreted version of the same GPR profile with prominent reflectors annotated by black lines. The basal reflector at ~3.5–5 m is interpreted as the base of the peat bog.

Table 1
Samples used in this study including deposit type and median (Dx (50)) for the potential source sediments.

Name	Location	Deposit Type	Dx (50)
Source Samples			
AS01	57°13′31.00″N, 13°51′4.99″E	Sand dune bordered by glaciofluvial sediments	33
AS02	57°13′55.99″N, 13°51′8.99″E	Sand dune bordered by glaciofluvial sediments	149
AS03	57°13′55.99″N, 13°51′10.00″E	Sand dune bordered by glaciofluvial sediments	146
AS04	57°14′24.00″N, 13°51′31.99″	Sand dune bordered by glaciofluvial sediments	199
AS05	57°14′22.99″N, 13°51′33.00″E	Sand dune bordered by glaciofluvial sediments	195
AS06	57°14′54.99″N, 13°52′19.99″E	Sand dune bordered by glaciofluvial sed. and peat	157
AS07	57°15′6.00″N, 13°52′32.00″E	Sand dune bordered by glaciofluvial sediments	198
AS18	57°16′49.00″N, 13°50′51.00″E	Sand dune bordered by glaciofluvial and river sediments, coarse silt-fine sand	139
AS19	57°17′30.99″N, 13°50′49.99″E	Sand sheet	168
AS20	57°16′1.99″N, 13°49′33.99″E	Sand dune bordered by glaciofluvial sediments	166
AS21	57°16′4.00″N, 13°49′36.00″E	Glaciofluvial sediments	167
AS22	57°16′25.99″N, 13°47′22.99″E	Sand sheet	63
SMT1-0	57°17′14.93″N, 13°56′32.89″E	Sand dune, crest	211
SMT1-1	57°17′9.61″N, 13°55′6.59″E	Sand dune, crest	178
SMT1-2	57°17′7.95″N, 13°54′59.55″E	Sand dune, crest	175
SMT1-3	57°16′59.26″N, 13° 54′35.89″E	Sand dune, crest	165
SMT1-4	57°16′48.44″N, 13°54′25.96″E	Sand dune, crest	170
SMT1-5	57°16′36.18″N, 13°54′27.99″E	Sand dune, crest	183
SMT1-6	57°16′31.91″N, 13°54′15.12″E	Sand dune, stoss slope	157
SMT1-7	57°16′30.13″N, 13°54′3.23″E	Sand dune, crest	148
SMT1-8	57°16′29.34″N, 13°53′53.41″E	Sand dune, stoss slope	178
SMT1-9	57°16′23.95″N, 13°53′41.59″E	Sand dune, stoss slope	156
SMT1-10	57°16′19.43″N, 13°53′22.70″E	Sand dune, crest	152
SMT1-11	57°16′19.31″N, 13°53′6.33″E	Sand dune, crest	162
SMT1-12	57°16′7.34″N, 13°53′5.85″E	Sand dune, slipface	189
SMT1-13	57°16′1.48″N, 13°52′50.40″E	Sand dune, slipface	167
SMT1-14	57°15′57.42″N, 13°52′37.04″E	Sand dune, crest	167
SMT2-1a	57°15′27.21″N, 13°50′3.85″E	Sand dune	172
SMT2-1 b	57°15′27.21″N, 13°50′3.85″E	Sand dune	151
SMT2-2	57°16′14.45″N, 13°50′23.51″E	Sand dune	151
Peat Sequences			
SMS_{2008}	57°13′37.29″N, 13°55′17.15″E		
SMS_{2018}	57°13′38.22″N, 13°55′10.86″E		
SMDS	57°16′37.70″N, 13°55′30.86″E		
SMDN	57°17′7.69″N, 13°54′8.79″E		

2.4. Characterization of potential source sediments and peat ash samples

All bulk potential source samples were measured for grain size using a Malvern 3000 laser diffractometer. We present only the median values of these analyses (Dx (50)). Bulk samples were size fractionated by sieving into three (AS, n = 12: <38, 38–63 and >63 μm) or four size fractions (SMT, n = 18: <38, 38–63, 63–125 and >125 μm) following the Wentworth size classes for clay, silt, very find sand and fine sand. The bulk samples and the individual size fractions were thereafter analysed by FTIR-ATR.

Peat cores were sub-sampled in continuous 1 cm slices using a stainless-steel knife. From each slice a cube was cut to be used for bulk density analysis. The sub-samples were all then freeze-dried. Cubes were weighed and their volume was estimated using callipers. The bulk density was used to align the cores to acquire a composite sequence depth of 427 cm. Dry ashing of peat samples was performed every 2–3 cm and follows Sjöström et al. (2019). Samples were combusted at 500 °C overnight and results expressed as a percentage of the dry weight of the sample at 105 °C.

2.5. Age modelling

A total of 5 ^{14}C dates on plant macrofossils from the SMDS sequence were measured at the Tandem Laboratory, Uppsala University (Ua) (Table 2). The age-depth model was obtained using Bacon (Blaauw and Christen, 2011), version 2.5, which includes the IntCal20 ^{14}C calibration curve (Reimer and Reimer, 2020, Fig. 2). Peat accumulation rates (PAR) were calculated using the bulk density and the number of years per sample as given by Bacon.

2.6. FTIR-ATR

Peat ash and potential source sediment samples (bulk and individual size fractions) were analysed by Fourier transform infrared spectroscopy, using a Thermo Scientific™ FTIR equipped with an iS7 ATR device with a single-reflection diamond crystal at the SLAM Laboratory at the Department of Geological Sciences, Stockholm University. All labware and the ATR-diamond were cleaned with ethanol between each sample or by using compressed air whenever possible. The measurements were obtained for the mid-infrared wavelength spectral range of 4000–400 cm^{-1} (2.5–25 μm) at a resolution of 4 cm^{-1}. A background was measured before each sample (Gåling, 2019).

Reference spectra for major minerals (quartz, microcline, orthoclase, albite, anorthite, muscovite, biotite, calcite and amphibole) were obtained from the RRUFF database (http://rruff.geo.arizona.edu). Second derivative spectra of the sediment samples, peat ash and reference minerals were obtained using the {*andurinha*} R package (Álvarez-Fernández and Martinez-Cortizas, 2020). Second derivative IR spectrum can enhance the MIR spectral resolution and amplify tiny differences in IR spectra. Many differences poorly visible in FTIR spectra such as frequency position, information on the width and the maximum absorption intensity become clearer. As part of the {*andurinha*} routine all data are standardised using Z-scores. The inspection of the spectra showed that almost all

Table 2
Age dating information for the SMDS sequence.

Sample (cm)	Laboratory no.	Material Dated	14C yr ± 1SD	Calibrated Age Range (yr)
108	Ua-61551	Seeds, *Sphagnum* species	961 ± 29	792–925
182	Ua-61552	*Sphagnum* species	1897 ± 29	1726–1884
262	Ua-63972	*Eriophorum*/sedges (*sensu lato*) remains	2461 ± 29	2405–2620
374	Ua-63971	*Sphagnum* stems and leaves	3701 ± 29	3969–4099
426	Ua-61510	Insect remains, *Eriophorum* remains	4292 ± 35	4825–4961

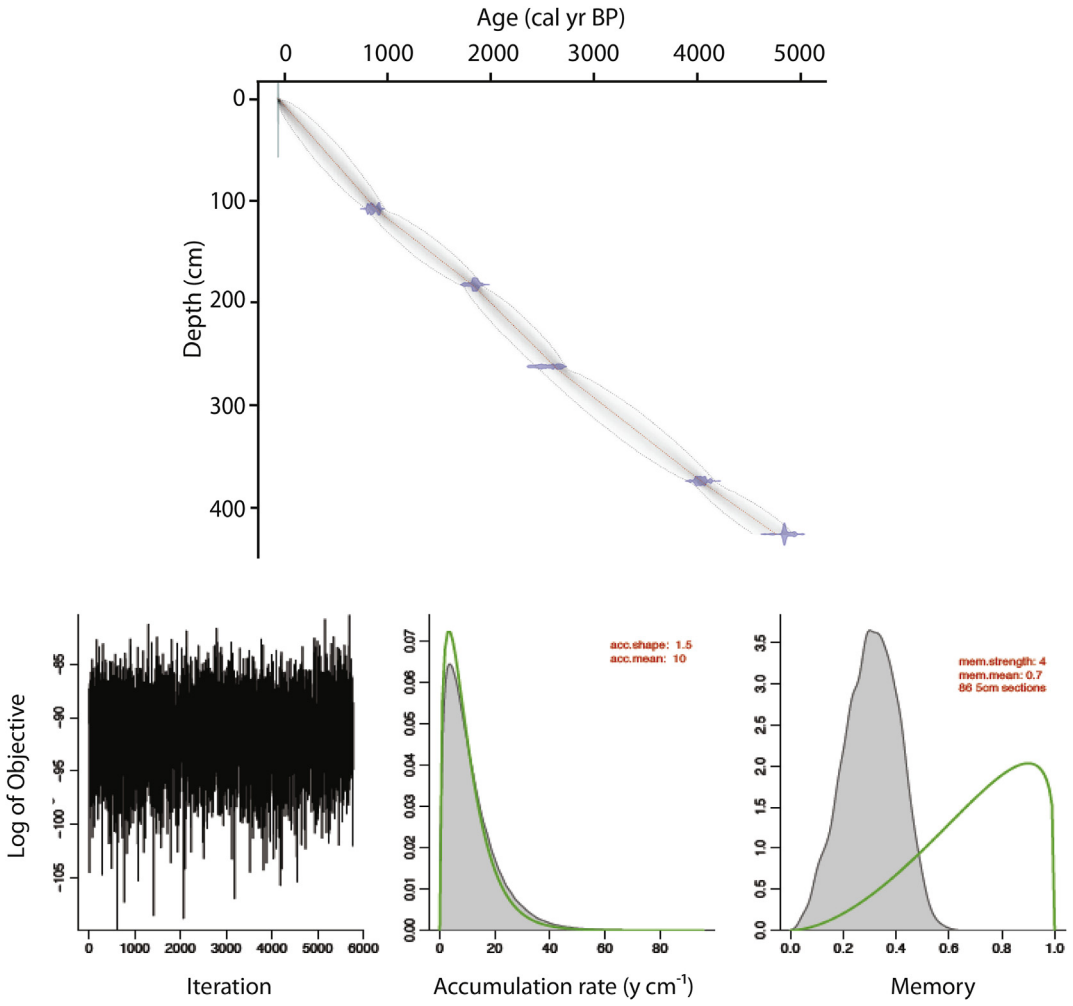

Fig. 2. Age-depth model for the SMDS sequence. The grey scale indicates the likely age-depth models with 95% confidence range. Calibrated distributions of the five ^{14}C dates (blue) are used to establish the weighted mean (red dotted line). Below is information about the model including the quality of the iteration, the predicted (grey shape) versus actual mean (green line), and values used in the a priori information in the Bayesian approach (Blaauw and Christen, 2011).

samples showed no or very low absorbance in the 4000-1900 cm^{-1} region (SD Fig. 2). Therefore, further descriptions and statistical procedures are based on the 1900-400 cm^{-1} region alone.

2.7. XRF core scanning (XRF-CS)

We used a method developed in-lab for analysing very small sub-samples for elemental variation using an Itrax XRF Core Scanner from Cox Analytical Systems (Gothenburg, Sweden) at the SLAM Laboratory. Sample holders were constructed by drilling a well into a solid piece of plastic. The interior dimensions of the sample well (10 × 3 mm) are larger than that of the X-ray beam (8 mm × 200 μm) and 4 mm deep, providing enough sample so that the X-rays do not reach the underlying plastic. The holders were first acid cleaned and then peat ash samples were packed into the holders using a stainless-steel spoon. Each holder was then laid on a custom built plexi-glass tray. This tray was placed on the sample stage and scanned like a normal core. During data processing all spectra measured on plastic were removed and an average calculated. The XRF measurements for this study were made using a Mo tube set at 30 kV and 50 mA at a step size of 500 μm (resulting in 2–5 measurements per sample) and a dwell time of 25 s.

2.8. Statistical analysis and modelling

A PCA was performed on the IR measurements (sediment and peat ash samples separately) using transposed data matrices (i.e., wave numbers in rows, samples in columns), correlation matrix

and a varimax rotation. With this approach, each sample spectrum is decomposed into a few scores' spectra (positive scores indicate MIR absorbance values above average and negative ones indicate MIR absorbance values below average), each accounting for a given proportion of the sample's spectral variation. This way, the scores enable the identification of the constituents of the samples responsible for each principal component (Cp). Both the whole spectrum of scores and peak values in a Cp can be compared to those of the reference minerals to aid in identification. In the transposed PCA each sample is assigned a loading value for each component, and as we used the correlation matrix, the square of the loading (i.e., its partial communality) represents the proportion of the samples' MIR spectral variance that is accounted for by each component. Variations in partial communalities can be taken as a proxy for changes in the relative abundance of the compounds/minerals along the peat core (Martínez-Cortizas et al., 2021a). However, it is worth noting that the proportion of MIR spectral variance of a mineral in a sample cannot be directly equated to the amount of that mineral present in the sample. In the way the variance is extracted in the PCA, the first component certainly represents the most commonly occurring/abundant mineral in the set of samples analysed. The order of the remaining components does not only depend on the minerals' abundances, but also on the overall area of the spectrum they cover (i.e., larger areas will produce a larger number of covarying absorbances) and possible overlapping effects with other minerals' spectra. Calibration with reference materials provides a way to obtain actual contents (e.g., Bosch-Reig et al., 2017; Grunenwald et al., 2014; Kaufhold et al., 2012; Müller et al., 2014), but this approach was not followed here due to the complexity of the mineral mixtures.

PCA was also used to explore the XRF-CS elemental data but based instead on a direct matrix (i.e., samples as rows, elements as columns). Elements with a high signal-to-noise ratios and relevance to the study were selected for inclusion. Prior to the PCA all data were transformed using Z-scores to deal with scaling effects. A PCA was then performed in correlation mode with a varimax rotation using the JMP Pro 14 software. Cp were extracted until they explained at least 85% of the variance in the data.

To infer the timing of discrete changes in the peat paleostorm proxies, changepoint modelling was applied (see Gallagher et al., 2011). This approach allows us to infer the location of changepoints (i.e., discontinuities where the mean of the data changes abruptly) without needing to specify in advance how many changepoints there are or where they are located. Furthermore, the approach does not require a priori knowledge of the noise in the observed values, but allows us to infer a noise distribution for each dataset. This noise can arise from analytical procedures and/or be introduced due to local geological or environmental processes. The approach implements a Bayesian transdimensional Markov chain Monte Carlo (MCMC) algorithm to propose many potential solutions (with different numbers and locations of changepoints and noise estimates), which are either accepted or rejected, based on simple probabilistic rules. One attractive feature of the Bayesian approach is that it naturally balances the requirement of fitting noisy data while avoiding an unnecessarily complex changepoint structure. If we anticipate the same changepoint structure (number and locations of changepoints), the approach can be implemented on single datasets in turn and the inferred changepoint structures compared visually. Alternatively, we can model multiple datasets simultaneously, noting that the magnitude and sense of the change can vary between datasets. This approach does not require the data to be sampled from the same depths/ages. An advantage of jointly modelling multiple datasets is that the common signal will tend to be reinforced while the noise component tends to cancel out (as it is generally random and independent across datasets). This again reduces the possibility of over-interpreting the changepoint structure. The output of the changepoint modelling method includes probability distributions on the number and location of changepoints, on the noise for each dataset and the inferred mean signal as a function of depth/age for each dataset. We note also that the inference of changepoints as a function of time assumes that the age models are reliable across the different datasets.

2.9. Powder X-ray diffraction (pXRD) analysis and rietveld phase quantification

To verify the mineral composition, a small number of peat (n = 3) and potential source sediments (n = 3) were analysed by pXRD at the Swedish Museum of Natural History, Stockholm. Due to widely different OM content of the potential source sediments (1.3–2.8%) and peat samples (~98%), different pre-treatments were applied. The source samples were analysed directly after washing in deionized water, while the peat samples were prepared following the protocol of Sjöström et al. (2019). All samples were milled into a fine powder prior to analysis. Analysis was conducted in a PANalytical XRD system (X'Pert^3 Powder) equipped with a multi-detector. The samples were analysed from 5 to 70° 2θ, with CuKα radiation at 45 kV and 4 mA, passing through a curved graphite monochromator, fixed divergence and receiving slits (1°), step size 0.0017° and 38 s count time. Processing of the results (determination of background, peak and phase identification quantification of relative occurrence) was conducted in HighScore 4.6, a PANalytical software (Degen et al., 2014), hosting a reference mineral database (ICDS database 2012) and Rietveld quantification (Rietveld, 1969). Quantification was restricted to results between 5 and 55° 2θ, using the default HighScore settings (Degen et al., 2014).

3. Results

3.1. Potential source sediment and peat properties

With the exception of two samples, the median grain size of the potential source sediments falls between 139 and 211 μm (average and standard deviation: 168 ± 18 μm, all standard deviations given as 1σ, n = 30). Only AS01 and AS22 have significantly lower median grain sizes of 33 and 63 μm, respectively (Table 1).

The bulk density of the peat ranges from 0.03 to 0.14 g cm^{-3} with an average value of 0.07 ± 0.02 g cm^{-3} (n = 408; Fig. 3). The highest bulk densities are found at the base of the sequence up to 4100 cal yr BP (maximum of 0.14 g cm^{-3}). A second increase to nearly the same values is observed from 3405 to 3240 cal yr BP with a maximum recorded at 3355 cal yr BP (0.12 g cm^{-3}). A more noticeable period of higher bulk densities is observed from 2310 to 2035 cal yr BP (ranging from 0.08 to 0.10 g cm^{-3}). Thereafter peaks from a background of ~0.05 g cm^{-3} are centred on 1525 (0.09 g cm^{-3}), 1020–870 (0.08–0.09 g cm^{-3}), 730–650 (ranging from 0.07 to 0.09 g cm^{-3}) and 370 (0.08 g cm^{-3}) cal yr BP. Bulk densities then increase gradually from 335 cal yr BP to present (0.11 g cm^{-3}). PAR range from 26 to 123 g m^{-2} yr^{-1} having an average value of 60 ± 19 g m^{-2} yr^{-1} (n = 407). Because the age model is near-linear the PAR shows the same variations as the bulk density. The ash content of the samples range from 0.6 to 7.1%. In general, the majority of samples have very low ash content. The main exceptions are the sample at 3620 cal yr BP, which has a value of 7.1%, and the samples representing the last 250 years (2.2–5.2%). If these samples are excluded the average ash content is low, 1.0 ± 0.2% (n = 154), with the samples at the base of the sequence

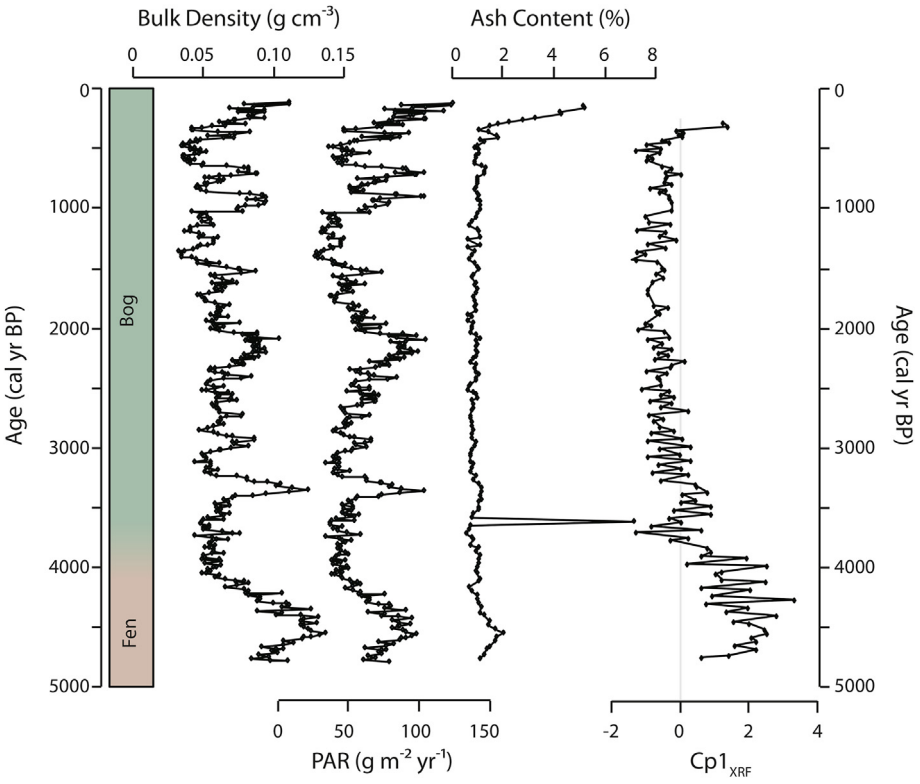

Fig. 3. Stratigraphy, bulk density, net peat accumulation rates (PAR), ash content and principal component 1 ($Cp1_{XRF}$) for the SMDS sequence.

between 4730 and 4400 cal yr BP showing slightly higher values. The full raw data for peat properties, FTIR-ATR and XRF-CS are available at https://bolin.su.se/data/kylander-2022-store-mosse-1.

3.2. FTIR-ATR

The individual IR absorbance spectra of the potential source sediment (bulk) and peat ash samples show a generally consistent pattern within each sample type (Fig. 4). The second derivative of the average absorbance spectra allows us to determine the precise location (wavenumber) of the most important peaks in the IR spectra, and it is particularly helpful to discriminate overlapping vibrations. Relatively high absorbances were obtained in the 1200-850 cm^{-1} region and in the <500 cm^{-1} region, with lower absorbances in the 800-500 cm^{-1} region. Relative maxima can be seen at approximately 1170–1150, 990–1000, 900 (shoulder), 800–770, 720, 690, 580 and 520 cm^{-1}. The second derivative spectra enables identification of significant peaks that can be attributed mostly to silicates through comparison with spectra from the RRUFF database (SD Fig. 3): quartz (1200, 1165, 1084, 1055, 798, 777, 692, 519,496 and 459 cm^{-1}); K-feldspar (microcline and orthoclase: 1136, 1034, 1001, 985, 723, 649, 606, 561 and 532 cm^{-1}); plagioclase (albite: 1084, 1034, 985, 760, 742, 723, 649, 606, 584, 532, 476 and 459 cm^{-1}; anorthite: 1140, 985, 777, 760, 723, 606, 567, 532, 519 and 436 cm^{-1}); and mica (muscovite and biotite share vibrations at 640, 519 and 457 cm^{-1} but muscovite also has vibrations at 1030, 910, 742 and 640 cm^{-1}). The spectra of the medium and fine fractions are similar to those of the bulk and coarse fraction, suggesting a comparable mineralogy. The main difference was found for the finer fractions, as they show low absorptions centred at 1620 and 1400 cm^{-1}. These may correspond to organic compounds (aromatic + N-containing compounds and aliphatics) and iron oxides (which show a low absorbance at around 1630 cm^{-1}).

The spectra of the peat ash show very high absorbance in the 1200-900 cm^{-1} region, with maxima at 1100 and 1050 cm^{-1}, and a shoulder at 1000 cm^{-1} (Fig. 4). High absorbance also occurs in the 1500-1370 cm^{-1} region, peaking at 1480 (shoulder) and 1410 cm^{-1}. Again, better peak identification can be done based on the average second derivative spectrum, which indicates the presence of quartz (absorbances in the 1200-1050 cm^{-1} region, 798 and 777 cm^{-1}) and, possibly, of other silicates. For example, peak absorbances of K-feldspar (microcline and orthoclase), albite and mica occur at 980-1000 cm^{-1} and that of anorthite at around 900 cm^{-1} (SD Fig. 3). A large part of the MIR spectral signal corresponds to minerals that were not detected in the source sediments, such as calcite (1412, 874 and 712 cm^{-1}) and anhydrite (1101, 677 and 592 cm^{-1}).

As indicated in the methods section, PCA was applied separately to the potential source sediments (bulk and individual size fractions) and the peat ash samples, including the spectra of the reference minerals. Six principal components accounted for 98% and 99% of the MIR spectral signal of the potential source sediments (denoted by Cp_{Source}) and peat ash samples (denoted by Cp_{Peat}), respectively. The reference minerals showed large loadings in the first four components of the sediments: quartz in $Cp1_{Source}$, mica (muscovite and biotite) in $Cp2_{Source}$, K-feldspars (microcline and orthoclase) and albite in $Cp3_{Source}$ and anorthite in $Cp4_{Source}$ (Fig. 5). $Cp5_{Source}$ showed two major high absorbance regions centred at 980–930 and 760 cm^{-1} while component $Cp6_{Source}$ showed a low absorbance at 1630 cm^{-1} and higher between 590 and 470 cm^{-1}, which may correspond to iron oxides. Quartz, mica, K-feldspar and Ca-plagioclase also showed large loadings in the peat ash samples (Fig. 5), accounting for the MIR spectral signal of four of the components ($Cp2_{Peat}$, $Cp4_{Peat}$, $Cp5_{Peat}$ and $Cp6_{Peat}$). Components $Cp1_{Peat}$ and $Cp3_{Peat}$ did not correspond to any of the reference silicates.

The scores' spectra of most of the extracted components match well with the absorbance and second derivative spectra of the

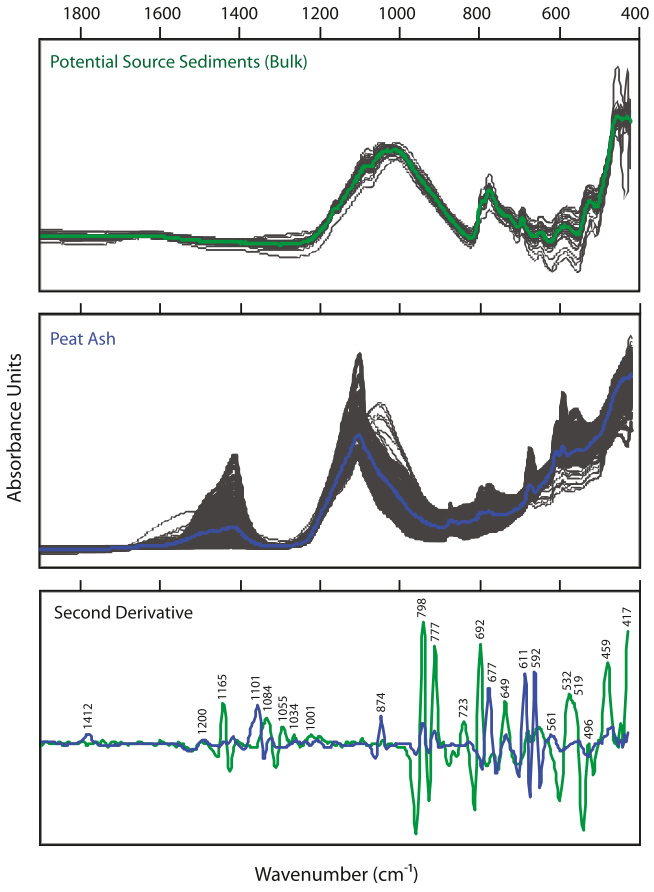

Fig. 4. Absorbance spectra of the bulk potential source sediment and peat ash samples (the coloured line of each panel corresponds to the average spectrum). Second derivative of the average spectra are also included (the colour of the lines corresponds to those of the average absorbance spectra).

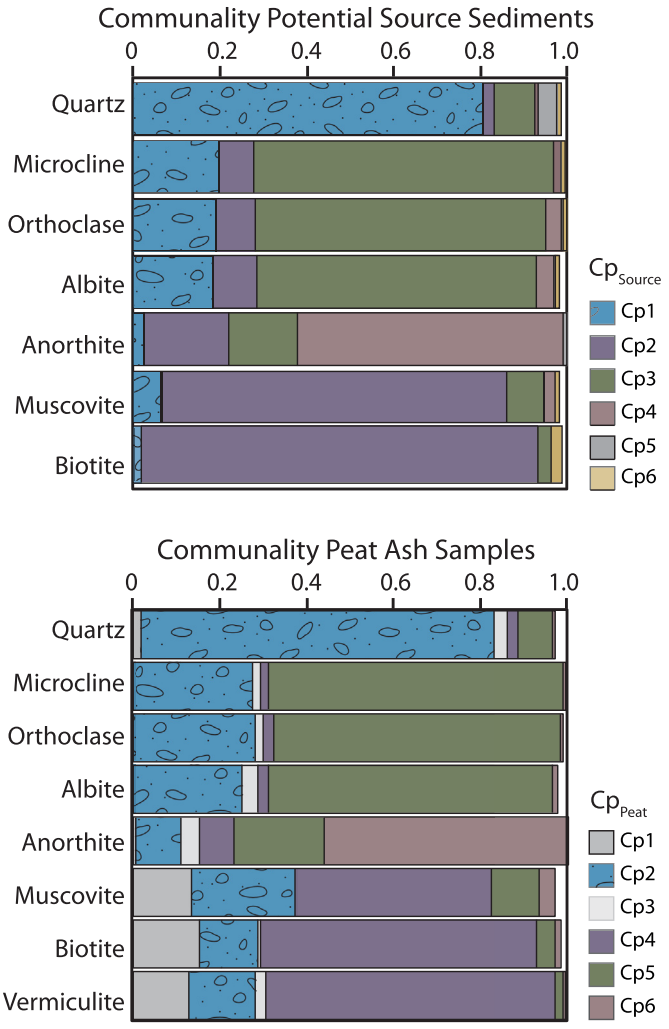

Fig. 5. Fractionation of the communalities for the reference minerals for the bulk potential source sediments and peat ash samples.

reference minerals (SD Figs. 4 and 5). For mica, the sum spectrum of muscovite and biotite fits better the $Cp2_{Source}/Cp4_{Peat}$ scores' spectrum, but the biotite signal seems to dominate. The feldspar signal of $Cp3_{Source}/Cp5_{Peat}$ fits better with K-feldspar (microcline) and $Cp4_{Source}/Cp6_{Peat}$ matches with the Ca-plagioclase (anorthite). In the peat ash samples, $Cp1_{Peat}$ scores' spectrum does not match any of the references (i.e., silicates). $Cp3_{Peat}$, on the other hand, fits with the anhydrite spectrum. These minerals, as well as other carbonates, and Ca-rich sulphates, oxides and silicates were extensively found in biomass ash (Vassilev et al., 2012). Thus, these latter two components reflect minerals formed during dry ashing and will not be further discussed here.

The graph of the partial communalities shows that the IR signal of the sediment samples (Fig. 6) is dominated by quartz ($Cp1_{Source}$), followed by mica ($Cp2_{Source}$), microcline/albite ($Cp3_{Source}$) and small proportions of anorthite ($Cp4_{Source}$). With decreasing grain size, the percentage of the MIR spectral signal accounted for by quartz ($Cp1_{Source}$) decreases (coarse 72 ± 13% vs fine 32 ± 11%, n = 30 both), while micas ($Cp2_{Source}$), Ca-feldspar ($Cp4_{Source}$) and the signal attributed to iron oxides increases ($Cp6_{Source}$) (coarse 13 ± 9% vs fine 48 ± 15%, coarse 2 ± 2% vs fine 5 ± 2%, coarse 0.2 ± 0.3% vs fine 3 ± 2%, respectively). K-feldspar ($Cp3_{Source}$) does not show a clear grain-size pattern, but its signal is slightly higher in the medium fraction (coarse 11 ± 6%, medium 14 ± 5% n = 18, fine 10 ± 6%). The IR signal of the peat ash samples shows a more varied composition. The minerals formed during peat ashing ($Cp1_{Peat}$ and $Cp3_{Peat}$) account for 20%–90% of the total communality (grey shades, Fig. 7). By far the most important mineral in the record is quartz ($Cp2_{Peat}$, up to 71% of the total communality in parts), followed by mica ($Cp4_{Peat}$, <9%), K-feldspar ($Cp5_{Peat}$, <9%) and Ca-feldspar ($Cp6_{Peat}$, <1%). It is worth reminding the reader here that while variations in the partial communalities with depth/age do reflect *relative changes* in the abundance of the minerals, they cannot be directly equated to the amount of mineral in the samples without a proper calibration (see Section 2.8).

The temporal variability in SMDS's mineral content is more clearly plotted using the individual partial communalities (Fig. 8). There is a weak, generally increasing trend in quartz ($Cp2_{Peat}$) from the base of the profile upwards. At the very top of the profile from 250 cal yr BP to present, quartz ($Cp2_{Peat}$) increases considerably, accounting for up to 71% of the observed MIR spectral variance in the peat ash. Peaks are centred on 4615, 4445, 4190, 3265, 2530, 2330, 2130–1965, 1450, 900, 695 and 390 cal yr BP. The mica ($Cp4_{Peat}$) profile has peaks centred on 4615, 4515, 3330, 2945, 2385, 2160–2080, 1805, 1325, 1005, 650, 405 and 240 cal yr BP. Mica ($Cp4_{Peat}$) generally mimics quartz ($Cp2_{Peat}$) but, interestingly, there are a number of instances where peaks are slightly out of step with each other, with mica ($Cp4_{Peat}$) both leading and lagging behind quartz ($Cp2_{Peat}$) and K-feldspar ($Cp5_{Peat}$). Conversely, quartz ($Cp2_{Peat}$) and K-feldspar ($Cp5_{Peat}$) have similar records (r = 0.65). Differences are seen at the base of the profile, where two of the

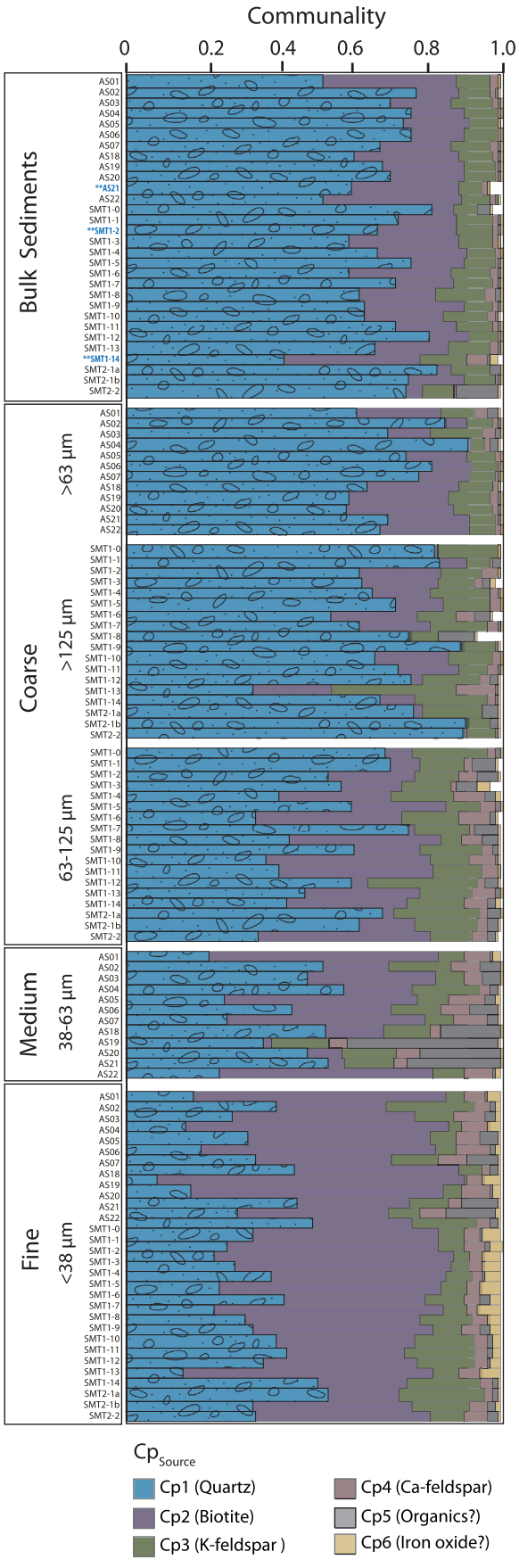

bottom peaks in quartz ($Cp2_{Peat}$) present themselves as a single sustained increase in K-feldspar ($Cp5_{Peat}$; 4475 to 4190 cal yr BP). In addition, the relative importance of the peaks at 2130-1965 cal yr BP is greater in the K-feldspar ($Cp5_{Peat}$) profile and inputs also increase more noticeably between 1770 and 1640 cal yr BP. The profile for Ca-feldspar ($Cp6_{Peat}$) is unique in comparison to the other mineral profiles. Peaks are centred on 4375–4120, 2510, 2280–2060, 1830, 1615, 1510, 1325–1260, 1110, 670 and 405 cal yr BP.

Changepoint modelling was applied to both quartz ($Cp2_{Peat}$) and K-feldspar ($Cp5_{Peat}$) profiles, although the top 250 cal yr BP was excluded due to suspected anthropogenic impacts (see Discussion). For quartz ($Cp2_{Peat}$) peaks in the average weighted function were identified at 4470–4410, 3325–3180, 2180–1920, 990–835, 710–660 and 410-355 cal yr BP (Fig. 9). Peaks in K-feldspar ($Cp5_{Peat}$) were recognised at 4480–4165, 3315–3180, 2150–1930, 1480–1435, 945–865 and 720-660 cal yr BP.

3.3. pXRD

The pXRD mineral results show that the potential source sediments are dominated by quartz, alkali feldspar and plagioclase feldspar, together with occurrence of mica (biotite) and carbonate (calcite and/or dolomite) minerals (Table 3). The uppermost peat ash sample (280 cal yr BP) is dominated by quartz, alkali feldspar and plagioclase, together with occurrence of mica and a layered double-hydroxide (LDH). The peat ash sample at 1985 cal yr BP is dominated by quartz, plagioclase and LDH, together with occurrence of mica and hematite, while that at 3495 cal yr BP is dominated by LDH and carbonates, with the presence of quartz and plagioclase.

3.4. XRF-CS

XRF-CS measures only relative changes in elemental intensity and not absolute concentrations. These data are used as secondary support for our interpretations. Based on analytical performance (counting statistics) Al, Si, Ti, P, K, Ca, Fe, Mn, Zn, Pb and Zr were analysed using PCA. The top seven samples were not included because of likely anthropogenic signal (see Discussion). Four Cp were extracted capturing 85% of the total variance in the dataset (denoted Cp_{XRF}; Table 4). $Cp1_{XRF}$ explains 26% of the variance in the data and is positively associated with Mn, Fe and Ca. $Cp2_{XRF}$ explains 25% of the variance in the data and represents the behaviour of Zr, Ti, Si and Al. $Cp3_{XRF}$ explains 19% of the data and describes the behaviour of P, K and Al. Finally, $Cp4_{XRF}$ accounts for 14% of the variance in the data and is associated with Pb and Zn.

Given the research question, the factor scores of $Cp1_{XRF}$ and $Cp2_{XRF}$ were plotted by age in order to investigate the changes in these components over time (Fig. 3). $Cp1_{XRF}$ shows higher values from the base of the profile up to 3835 cal yr BP and an increase in the topmost two samples. $Cp2_{XRF}$ has high basal values up until 4475 cal yr BP. The factor scores remain negative until 2410 cal yr BP with the exception of a peak centred on 3330 cal yr BP. Further excursions to positive values are seen at 2560, 2310, 2130, 2080, 1450, 1325, 1260, 1005–900, 710, 670, 405 and 390 cal yr BP (Fig. 8). The Si/Al ratio shows a weakly increasing trend moving towards the top of the profile and increases considerably from 250 cal yr BP to

Fig. 6. Fractionation of the communalities for the potential source samples for both bulk and individual size fractions. Note that the SM samples and AS samples had slightly different coarse fractions used where the former included <38, 38–63, 63–125 and >125 µm and the latter <38, 38–63 and >63 µm. For the SMT samples there was not enough material to analyse the 38–63 µm fraction. Samples in blue with an asterisk were analysed by XRD.

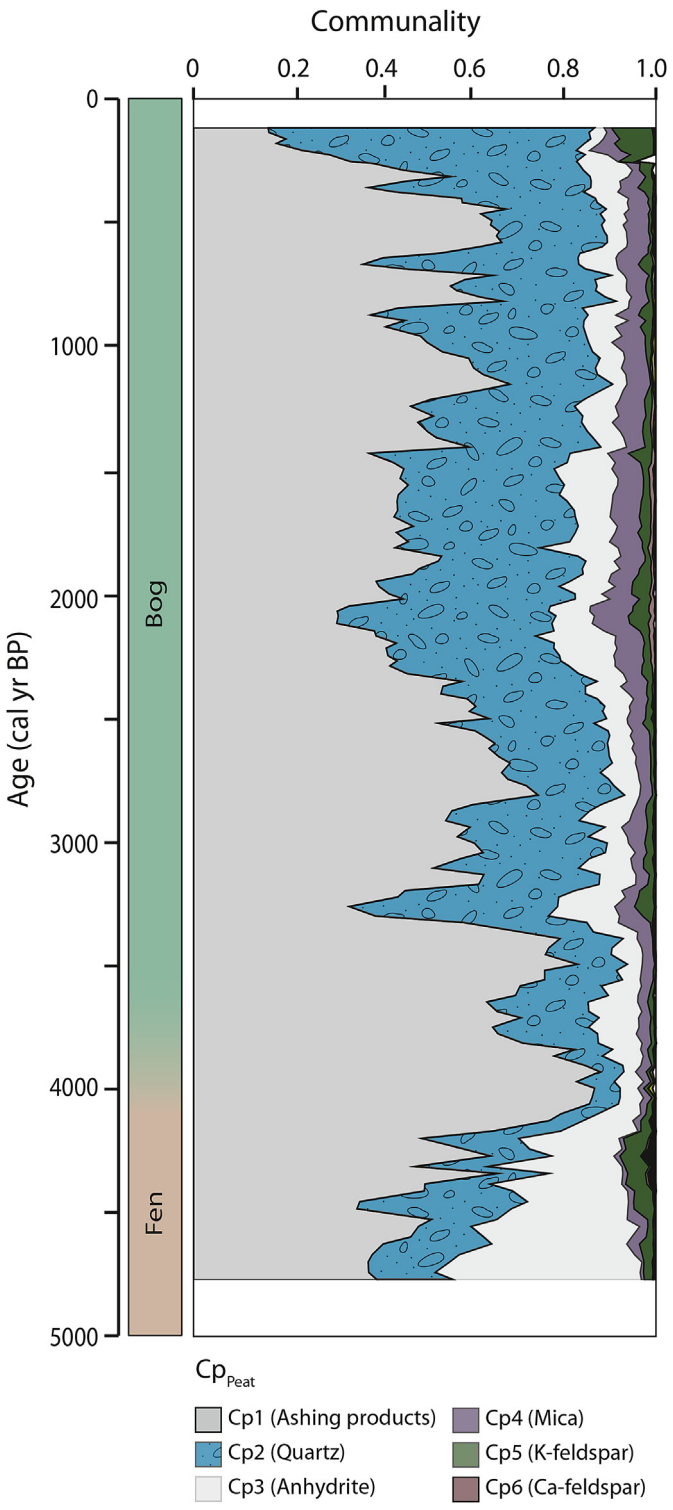

Fig. 7. Fractionation of the communalities for peat ash samples plotted by depth. The products of dry ashing (grey shades) do not contain any paleoclimatological information.

the top. Peaks are noted at 4445, 3330–3325, 2530, 1450, 900 and 710 cal yr BP.

Changepoint modelling identified peaks in the average weighted function of $Cp2_{XRF}$ at 4730–4425, 3345–3290, 2360–2075, 1050–860, 720–655 and 415-370 cal yr BP (again the top 250 cal yr BP was not included; Fig. 9). For Si/Al, peaks were dated to 4460–4435, 3360–3200, 1470–1445, 1050–845 and 410-380 cal yr BP.

4. Discussion

4.1. Characterising potential source samples

Although there have been several studies of Swedish dune chronologies, depositional wind regimes and a few grain-size analyses (e.g., Alexanderson and Bernhardson, 2019; Alexanderson and Fabel, 2015; Bernhardson et al., 2019; Bjermo, 2019), dune mineralogy has not been examined in-depth in recent years (Högbom, 1923, 1913; Hörner, 1927; Mycielska-Dowgiałło, 1993) and no geochemical investigations have been made. As mentioned previously, Store Mosse sits in a granitic terrain (SGU, 2022a). There is an abundance of glacial sediments in the area including till, glaciofluvial and glaciolacustrine sediments as well as aeolian deposits derived from these materials (SGU, 2022b). While it is hard to provenance these glacial materials, we expect till to be local/regional in nature (<80 km; Sohlenius et al., 2009) and glaciofluvial sediments are likewise transported relatively short distances (<50 km; (Alexanderson, 2022; Alexanderson and Murray, 2012). Given the N–S direction of the glacial striations in the region, these materials should be derived from areas to the north of Store Mosse where the bedrock is similarly felsic and often of the same age (SGU, 2022a, 2021). Therefore, we assume that the local source sediments are composed of mostly quartz and feldspars (microcline, orthoclase, albite, anorthite) with lesser amounts of amphibole and mica (muscovite, biotite, vermiculite; Wedepohl, 1995). The reference spectra of these minerals were included in the PCA of the IR analysis along with a range of other common minerals, e.g., calcite, based on previous studies in the area (Sjöström et al., 2020).

The PCA analysis on the IR signal of bulk potential source sediments shows that quartz ($Cp1_{Source}$) is most important, explaining >60% of the variance in all but four samples. We remind the reader that the extraction of the Cp is a function of both the actual mineral abundance and the total absorbance area of the mineral in the spectrum (1900-400 cm^{-1} in this case; see Section 2.8). Thus, the loading of mica onto the second component ($Cp2_{Source}$) is partly a result of its MIR spectral pattern (i.e., the total absorbance area of the mica spectrum is greater than that of feldspar and anorthite and has broader peaks in SD Fig. 4). Given the granitic surroundings, mica is expected to be a minor part of the deposited material. K-feldspars ($Cp3_{Source}$) and Ca-feldspars ($Cp4_{Source}$) explain the remaining variability in the bulk sample. The presence of these four minerals in the surrounding potential source sediments is unsurprising as these are all commonly found in aeolian deposits (Pye and Tsoar, 2009). Two phases possibly representing organic contributions and iron oxides were also found but explain very low amounts of the variance in the data and are not considered further. XRD analyses were made on three sediment samples (AS21, SMT1-2 and SMT1-14; Fig. 6). These data confirm that quartz dominates nearly 70% of the analysed materials (Table 3). As suspected, the feldspars (albite and K-feldspar) are more important than biotite revealing the previously raised artefact of the PCA extraction on IR data. Minor carbonate content was also recorded in two of the samples. The array of bulk potential source sediments does not appear to show any spatially consistent variability, which suggests (i) a limited and/or well-mixed source area that would support the idea of rather short glacial transport and (ii) effective sorting of the material and subsequent impact on the mineral composition. A summary of the nomenclature and interpretation of the Cp is given in Table 5. For the sake of simplicity we refer to the inferred mineral, rather than their Cp, in the discussion.

Generally, dunes are thought to be comprised of coarser-grained

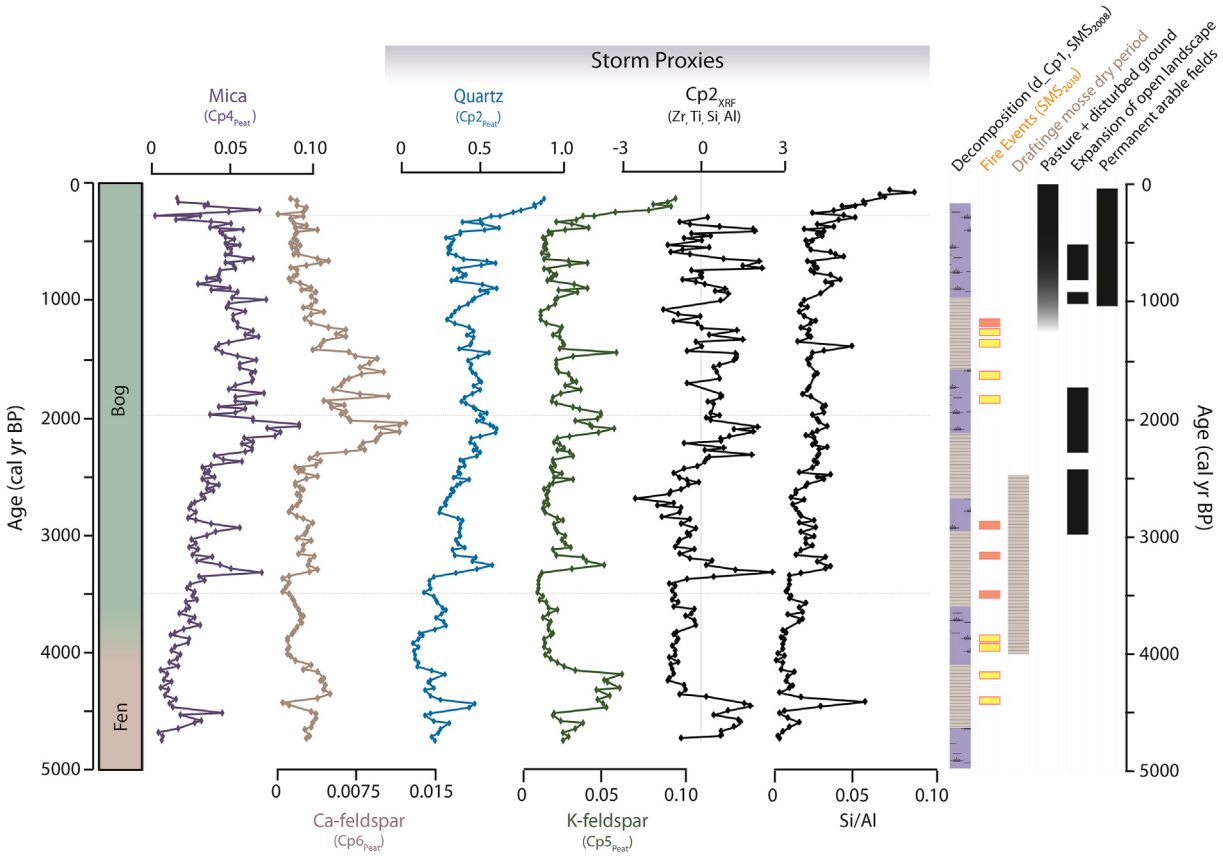

Fig. 8. Partial communalities of the minerals identified by FTIR-ATR analysis of the SMDS sequence representing relative changes in mica (principal component 4, $Cp4_{Peat}$) Ca-feldspar ($Cp6_{Peat}$), quartz ($Cp2_{Peat}$) and K-feldspar ($Cp5_{Peat}$). These latter two minerals, along with $Cp2_{XRF}$ and Si/Al from the XRF-CS elemental dataset, representing lithogenic inputs and grain-size changes, respectively, are used as storm proxies for the SMDS sequence. Increased storminess would see an increase in each of these proxies. The dashed lines show the depths where pXRD analyses were performed. The degree of peat decomposition gives insight into the bog hydrology, and by extension, effective humidity. We summarize changes in decomposition as derived from a study of the organic matter composition of the SMS_{2008}- sequence (d_Cp1 is the detrended first component from an FTIR analysis of the bulk peat representing shortterm peat decomposition). Periods of higher decomposition are linked to dry periods (horizontal hatching). These overlap fairly well in time with the four biggest charcoal events (>10% charcoal) observed in the SMS_{2018} sequence (red bars in column), which indicate local periods of fire activity (yellow shading is <10% charcoal). Drier periods at Store Mosse overlap with a period of very low peat accumulation/hiatus, and therefore dry conditions, at Draftinge mosse (horizontal hatching). Several indicators of anthropogenic activity are shown including pollen-based records of pasture and disturbed ground from Store Mosse itself as well as indicators of agriculture from Lake Avegöl, a site 70 km north-northeast. See text for references.

material (70–250 μm) in comparison to loess (silt, 10–70 μm) and aeolian dust (<10 μm; Pye and Tsoar, 2009). The majority of the potential source samples analysed here had median grain sizes between 140 and 210 μm (Table 1). This classifies these as fine sands and sands, which are within the expected range for this deposit type (Ahlbrandt, 1979). A previous study on the dunes at Store Mosse saw similar ranges, although these were taken at 70 cm depth or more (n = 5; 200–260 μm; Bjermo, 2019). Two samples, AS01 and AS22, have much lower median grain sizes (33 and 63 μm, respectively). This is likely linked to the amount of quartz (coarser grained), which explains slightly lower proportions of the MIR spectral variance in these samples (52%). According to the Quaternary deposit map (SGU, 2022b), AS22 is taken from a sand sheet. The smaller grain size may be linked to the genesis of the sediment or may just represent natural variability within the deposit. The sampling sites were selected based on available maps, which are low resolution in comparison to the size of the actual deposits. While loess has not been mapped in the area, the low median grain size of AS01 suggests that it could be present, as found in other inland dune systems in Sweden (Alexanderson and Fabel, 2015; Hörner, 1927; Stevens et al., 2022). The SMT1 samples have a slightly tighter range of median values (with perhaps the exception of SMT1-0) than the samples taken to the west of the bog, which could reflect a more heterogenous landscape cover.

There is a clear relationship between the IR-inferred mineralogy of the source sediments and certain grain-size fractions (Fig. 6). The AS samples were analysed first and fractionated into <38, 38–63 and >63 μm size fractions. Based on the observed trends in these data, we decided to analyse the SMT samples for four size fractions, adding on the coarser end (<38, 38–63, 63–125 and >125 μm). Unfortunately, despite a considerable amount of material, we did not have enough to analyse any of the 38–63 μm size fractions for the SMT samples. The bulk sample and the coarsest fractions have similar mineralogy with a slightly higher proportion of quartz in the latter (bulk: 67.9 ± 9.4%, >125 μm for SMT: 71.2 ± 14.1%, >63 μm for AS: 71.8 ± 10.5%). Mica clearly increases in the fine (<38 μm) fraction (47.9 ± 15.3%). The behaviour of K-feldspar is not as obvious but seems to show marginally higher average values in the medium coarse (63–125 μm) fraction for the SMT samples (14.9 ± 5.3%) and the medium (38–63 μm) fraction for AS samples (11.8 ± 4.1%). Because Ca-feldspar explains such a small part of the variance (1.4 ± 1.6%), it is hard to define any grain-size relationship, but a tendency towards finer sizes is suggested. A single coastal dune sample from Halland (~90 km to the southwest) was analysed for

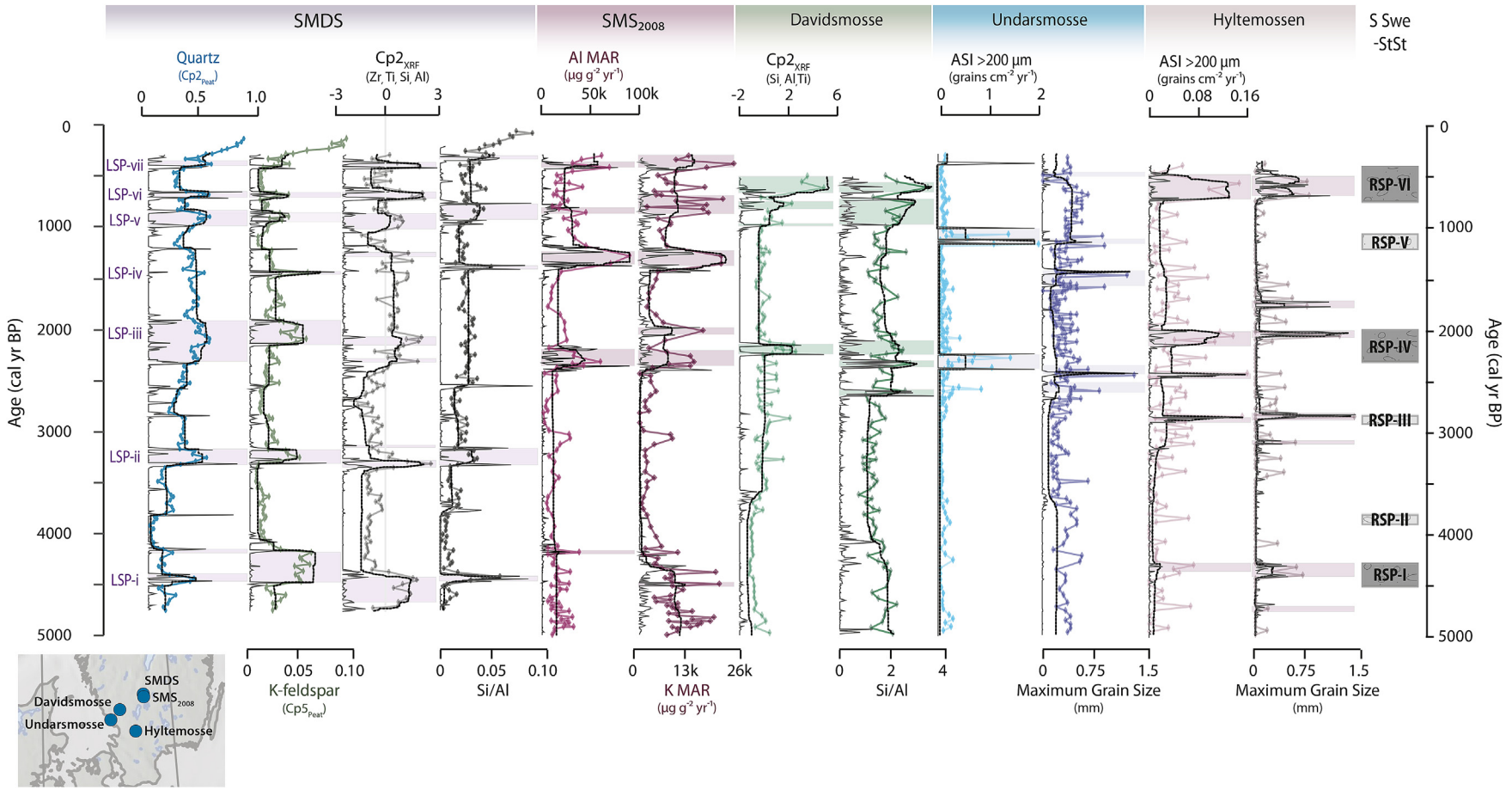

Fig. 9. Individual storm proxies from sites in southern Sweden starting from inland sites and moving southwest towards the coast with changepoint modelling applied to each proxy individually (left to right, see inset). For SMDS quartz (principal component 2, $Cp2_{Peat}$) and K-feldspar ($Cp5_{Peat}$) from the FTIR-ATR analysis as well as $Cp2_{XRF}$ and Si/Al from the XRF-CS elemental dataset were included. Although storm periods constrained by changepoint modelling of these four proxies individually vary in timing and duration, we have defined several local storm periods (LSP). These are compared with Al and K mass accumulation rates (MAR) from SMS_{2008}, a sequence taken ~5 km south of SMDS in the same bog complex. Davidsmosse is represented by $Cp2_{XRF}$ and the Si/Ti ratio from a multi-element XRF dataset. Finally, at the two coastal sites, Undarsmosse and Hyltemosse, the aeolian sand index (ASI) for grains >200 µm and the maximum grain size are used. The original data are shown in colour. Changepoint modelling was applied to all proxies individually and peaks in the inferred functions (black line) were constrained temporally using the changepoint structure (thin grey line) where higher values indicate a greater probability of a changepoint occurring. This information was used to identify stormier periods in individual proxy records (shaded boxes). To generate a regional storm stack for southern Sweden (S Swe-StSt), quartz and Si/Al from SMDS was modelled jointly with the other available storm proxies (excluding SMS_{2008}) to find common changepoints (SD Fig. 6). Those regional storm periods (RSP) periods with darker shades of grey, namely RSP-I, RSP-IV and RSP-VI, had slightly better agreement across the sites and proxies. See text for references.

Table 3
Minerals and relative occurrence (%) from pXRD results.

	Quartz	Alkali feldspar	Plagioclase feldspar	Mica	Carbonates	LDH	Hematite	R_{wp}
Source Samples								
AS21	68	15	16	[a]	0.7			14.7047
SMT1-2	70	15	15	[a]				14.2558
SMT1-14	68	15	16	[a]	0.7			14.4983
Peat Samples								
280 cal yr BP	50	21	27	1		2		17.0945
1985 cal yr BP	33		30	[a]		37	0.5	13.3085
3495 cal yr BP	9		13		20	58		11.8294

[a] presence, below 0.1% occurrence, LDH = layered double-hydroxide; R_{wp} is a discrepancy value between the data and the model (Toby, 2006).

Table 4
Variance explained by each principal component (Cp_{XRF}) and rotated (varimax) factor loadings. Data in bold show stronger relationships with loadings greater than 0.5.

Variable	$Cp1_{XRF}$	$Cp2_{XRF}$	$Cp3_{XRF}$	$Cp4_{XRF}$
Variance	2,9	2,8	2,1	1,6
Percentage	26,3	25,0	19,2	14,6
Cumulative %	26,3	51,3	70,5	85,1
Mn	**0.95**	−0.10	−0.11	0.16
Fe	**0.94**	−0.08	−0.16	−0.23
Ca	**0.87**	−0.24	0.11	−0.10
Zr	−0.16	**0.92**	0.02	0.00
Ti	−0.19	**0.80**	0.44	0.11
Si	−0.25	**0.70**	0.43	0.42
Al	−0.03	**0.69**	**0.56**	0.18
K	−0.42	0.26	**0.77**	0.08
P	0.12	0.17	**0.85**	0.03
Pb	−0.17	0.38	−0.13	**0.73**
Zn	0.04	−0.04	0.21	**0.87**

mineralogical content by size fraction. Quartz was found to dominate the coarse fraction (particularly >150 μm) and both plagioclase and alkali feldspars had the highest relative contributions in the fine (<38 μm) and medium (38–63 μm) size fractions (Sjöström et al., 2022), which agrees with what is observed here.

4.2. Peat deposit development

Previous paleoenvironmental work at Store Mosse by Svensson (1988) explored the peat age, thickness and macrofossil composition in the southern end of the deposit, some edge areas as well as peat cuttings in the northeast corner (Fig. 1). Based on findings from this earlier work, our studies have focussed on the thickest and oldest sections (5.5–7 m, up to 10,000 years old) in the southern bog complex (SMS_{2008}, SMS_{2018}; Kylander et al., 2013, 2016, 2018; Martínez-Cortizas et al., 2021b; Ryberg et al., 2022). From the GPR profiles that we have collected across Store Mosse and the map from Eller and Brenner (1912), there are clearly several thicker accumulations indicating that the peatland is formed in multiple sub-basins and/or initiation loci. The GPR profiles show that the SMDS basin is wide and flat, particularly in the area near the coring site, and leading up to the southern edge of the dunes (Profile-55, Fig. 1). The basal age of the SMDS sequence dates to 4755 cal yr BP. This can be compared to the basal date from an additional sequence taken to the north of the dunes, Store Mosse Dune North (SMDN), which returned a basal age of ~5300 cal yr BP. This suggests that after the drainage of the Ancient Lake Bolmen, peat accumulation started in the southern end of the wetland, the dunes were emplaced, and then the area north of Blådöpet began accumulating peat. The bottom depths for SMDS and SMDN are 472 cm and 486 cm, respectively, which is slightly shallower than those depths measured by GPR (~520 cm) and Eller and Brenner (1912; 580 and 550 cm, respectively). These offsets likely correspond to difficulties penetrating the base of the sequence with coring equipment compared to depth probes while the GPR was able to image the entire peat deposit in addition to the underlying strata.

The bulk densities and PAR of the SMDS sequence are higher at the base and decrease from ~4100 cal yr BP (Fig. 3). This fits well with what was observed in the field where visible *Sphagnum* remains were apparent above 385 cm; below this depth the material is much more decomposed. This density difference is captured in the GPR data, which show both the basal reflector from the basin as well as another reflector ~50 cm above this (Profile-55, Fig. 1). The ash content is <2% in this basal section indicating that very little inorganic input occurred. $Cp1_{XRF}$, which integrates the behaviour of Mn, Fe and Ca, has elevated factors scores up until 3835 cal yr BP. These elements are all mobile in the acidic conditions of a bog (Chesworth et al., 2006) and are expected to diffuse upwards from the basal sediment – like that seen in the $Cp1_{XRF}$ pattern. A drop in $Cp1_{XRF}$ thus provides another indication of ombrotrophy. Given this evidence, we are confident that the majority of the sequence is ombrotrophic and therefore atmospherically fed, with the fen-bog transition occurring ~4100 cal yr BP.

The ash content at the top of the SMDS sequence from 250 cal yr BP to present is up to 5%, which is off trend in comparison to the rest of the profile (Fig. 3). There is also an increase in the bulk density, PAR, quartz and K-feldspar (Figs. 3 and 8). Peat mining

Table 5
Summary of the different Cp for the local source sediments, SMDS peat ash and SMDS elemental analyses and their interpretation. Text in light grey denotes aspects not discussed in detail in the text due to low relevance for the study. Text in other colours shows thescheme used for the different minerals in Figs. 5–9.

	CpX_{Source} Source Sediments	CpX_{Peat} Peat Ash	CpX_{XRF}
Cp1	Quartz	*Minerals formed during ashing*	Mobile elements
Cp2	Mica	Quartz	Lithogenic input
Cp3	K-feldspar	*Anhydrite formed during ashing*	*Nutrient input?*
Cp4	Ca-feldspar	Mica	*Heavy metals?*
Cp5	*Organics?*	K-feldspar	
Cp6	*Iron oxide?*	Ca-feldspar	

occurred on an industrial basis in the first half of the 20th century at Store Mosse and within the same basin/lobe as the SMDS sequence. The construction of train tracks and roads as well as the extraction itself would have changed the local hydrology and certainly mobilised mineral material from the dunes in the northeast of the bog. This topmost increase is thus considered to be an anthropogenic signal and for this reason this part of the sequence was not included in the XRF PCA analysis or the changepoint modelling.

4.3. Characterising the inorganic fraction of the SMDS peat sequence

Previous studies show that the atmospherically derived inorganic material reaching the bogs in this temperate boreal region is dominanted by the most proximal mineral sources (Sjöström et al., 2022). This material comes from the weathering and erosion of diffuse sources of bedrock, till, aeolian sand dunes, glaciofluvial and glaciolacustrine sediments as well as soils formed on these. The closest potential mineral sources to SMDS are the sand dunes located ~1 km to the north of the sampling site (SMT1 samples; Fig. 1), which explains our focus on these deposits. While we recognise that mineral material from glaciofluvial deposits in the area may occur, the sampled sand sheets and dunes are likely derived from these deposits and as such, should have fairly similar mineralogy (but not grain size). Contributions from tills surrounding Store Mosse are likely to be less important with much coarser-grained material and thin soils, but again, the mineralogy is likely similar. A study from Davidsmosse, ~60 km to the southwest of Store Mosse, found that the same mineral phases occurred in the local till, glaciofluvial sediments and aeolian sediments (quartz > plagioclase feldspar > alkali feldspars > amphibole) together with some minor contributions from mica, chlorite and clays (Sjöström et al., 2022).

The inferred minerals from the IR analysis of the peat ash are the same as those of the potential source sediments, namely, quartz ($Cp2_{Peat}$), mica ($Cp4_{Peat}$), K-feldspar ($Cp5_{Peat}$) and Ca-feldspar ($Cp6_{Peat}$) (see Table 5 for nomenclature). Quartz dominates the profile accounting for up to 48% of the MIR spectral variance in the samples prior to 250 cal yr BP. At the very top of the sequence, which is thought to be anthropogenically impacted, this increases up to 71%. Mica is the second most important Cp but, again, this could be an artefact of the PCA extraction. pXRD analyses were made at 3495, 1985 and 280 cal yr BP (Table 3, dashed lines Fig. 8). Samples were washed prior to analysis to remove ashing products like those identified by the IR ($Cp1_{Peat}$ and $Cp3_{Peat}$). pXRD results showed, as with the sediment analysis, that quartz > albite > K-feldspar make up the majority of the sample with biotite and hematite found in small amounts (<0.1%). The presence of a carbonate secondary mineral, LDH, was also found at greater depths, which affected the relative amounts of the identified primary minerals. LDH, together with carbonates, have previously been identified in peat sequences in the same region and are likely of authigenic origin (Sjöström et al., 2020, 2022). Regardless, the dominance of quartz followed by feldspars is apparent.

As suggested previously, the top of the SMDS sequence is affected by human activities related to the mining of peat. Changes in coarse-grained input (sand flux and ASI) have been linked to both storms (e.g., Björck and Clemmensen, 2004; Orme et al., 2016; Kylander et al., 2020) and local deforestation and fires (Panait et al., 2019). Pollen analyses from the southern part of the bog complex at Store Mosse date the introduction of species associated with cultivation/pasture (Cerealia, *Plantago lanceolata* and *Rumex acetosa*) and disturbed ground (Chenopodiaceae and *Artemisia*) to sometime between 1440 and 980 cal yr BP (Svensson, 1988, Fig. 8). At Lake Avegöl, a site ~70 km north-northeast, an opening of the landscape was identified in pollen records between ~3000 and 2000 cal yr BP and ~1000 and 500 years ago. Permanent arable fields were established ~1000 years ago (Lagerås, 1996). It could be argued that there is a weak long-term increase towards the present in quartz, mica and $Cp2_{XRF}$, perhaps coupled to the opening of the landscape. Given the episodic nature of many of the observed mineralogical changes, however, they are likely not driven by anthropogenic activities. A charcoal record from SMS_{2018} identified a dozen fire events of which four were more substantial (>10% charcoal). The latter were dated to between 3900 and 2900 cal yr BP and 1200 cal yr BP (in red Fig. 8). For a fire to occur on the bog there must be fuel available and it must be dry enough for ignition by, for example, lightning. These fire events overlap in time with the presence of more decomposed peat seen in the SMS_{2008}-sequence, indicating dry conditions (using an FTIRbased proxy from the bulk peat; Martínez-Cortizas et al., 2021b). The former time bracket also overlaps with very slow peat accumulation/hiatus at the neighboring Draftinge mosse (~18 km to the southwest) from 4000 to 2480 cal yr BP. In examining the mineral profiles from SMDS, there does not appear to be any consistent link with fire events. However, drier conditions would increase the amount, but not necessarily the grain size, of mineral matter to the bog (Kylander et al., 2013, 2016).

The minerals that land on the bog surface are subject to weathering and associated secondary mineral formation and biological uptake. Thus, we observe only what remains after these processes are complete and the material is buried. There are differences in the susceptibility of different minerals where biotite and the plagioclase feldspars are more easily weathered than K-feldspar or quartz. The mineral profiles generally follow the same pattern and any differences may be a function of surface processes. Interestingly, quartz and mica variations show a slight temporal offset (50–100 years), e.g., those peaks dated to ~4520, 3330 and 650 cal yr BP (Fig. 8). The source sediment analysis suggests a clear relationship between quartz and coarse-grain sizes (>63 μm) and mica and fine size fractions (<38 μm). The offset in quartz and mica may stem from differences in wet/dry deposition and seasonality where finer fractions are more commonly removed via precipitation (Tegen and Fung, 1994). Another possibility is that this is due to a change in soil moisture or vegetation cover, where higher cover sees more fine-grained material than coarse being emitted. The Ca-feldspars also show a noticeable deviation from a rather stable background between 2280 and 1510 cal yr BP. This is a locally wet period at Store Mosse and points perhaps to a change in source area occurring after drier conditions ended or may be an expression of differential weathering rates in the bog.

The PCA of the XRF data grouped Zr, Ti, Si and Al onto $Cp2_{XRF}$ (Table 4). These elements are commonly hosted in zircon, rutile, quartz, feldspars and clay and are conservative lithophile elements often used as indicators of mineral input to bogs (e.g., Longman et al., 2017; Pratte et al., 2019; Shotyk et al., 2001; Weiss et al., 2002). While Si can be hosted in biogenic phases like diatoms and phytoliths, the association with elements hosted in conservative minerals suggests an inorganic origin for Si. This component is thus interpreted to represent the integrated signal of mineral input to the bog. $Cp2_{XRF}$ has the highest correlations with quartz ($r = 0.68$) and Ca-feldspar ($r = 0.64$), which agrees with the relative abundance suggested by the pXRD and confirms that these two minerals dominate the elemental signal (Table 3, Fig. 8). In a review of contemporary dust deposition, Si and Al concentrations were found to be relatively unchanged in comparison to the upper continental crust during dust transport, supporting the use of these elements to represent mineral deposition (Lawrence and Neff, 2009). The agreement between the MIR spectral data and $Cp2_{XRF}$, derived from two completely independent datasets also shows that

the fen section of the deposit does not greatly impact the PCA analyses. In an analysis of the elemental variations in different grain-size fractions of tills, glaciofluvial and dune samples, Sjöström et al. (2022) established Si/Al as a reliable proxy for grain-size changes. The agreement between the quartz and Si/Al profiles is strong ($r = 0.82$) despite, again, being based on two completely independent datasets.

4.4. Storm proxies at SMDS

One of the objectives of this work was to construct an inland paleostorm record based on the SMDS sequence. The rationale behind analyzing local source samples was to establish a link between the mineralogy and the grain size of the potential wind-blown material coming to the bog, in order to establish a proxy for changes in wind strength. There is a clear link between quartz and coarse grain sizes (>63 μm) in the potential source sediments (Fig. 6). This agrees with previous studies, where quartz tends to be concentrated in the coarser fractions in aeolian deposits (e.g., Ferrat et al., 2011; Pye and Tsoar, 2009; Sjöström et al., 2022). A review of contemporary aeolian dust fluxes shows that sands (>50 μm) make up 30% of the local aeolian deposition and tend to have higher proportions of quartz (>50%) than either regional (10–1000 km) or global dust (>1000 km; Lawrence and Neff, 2009).

Due to limitations in sample size it was not possible to measure the grain size of the SMDS peat ash and the observed quartz may be, in fact, fine grained. There are, however, a few observations that speak against this. First, the most proximal and likely source, the SMT1 dunes, are dominated by coarse grains with their median grain size falling between 139 and 211 μm (Table 1). Second, quartz is the dominant mineral in the bulk sediment and in the coarse fraction (Fig. 6). Finally, in the potential source sediments quartz abundance decreases with grain size while mica abundance increases. So, in the peat ash we might expect a tighter co-variation between quartz and mica if a majority of the quartz deposited in the peat was in the fine fraction. For these reasons we use quartz as an indicator of coarse-grained input driven by changes in wind strength.

The relationship between K-feldspar and different grain-size fractions was not as clear as for quartz, with some tendency towards enrichment in the 38–125 μm size interval (Fig. 6). As such, K-feldspar can be used as a general indicator of increased mineral input. It is also better suited than albite for comparison with data from local and regional records (described in the following section). $Cp2_{XRF}$ represents the integrated lithogenic signal coming to SMDS and is similarly used as an indicator of mineral input, while Si/Al is used as a grain-size indicator following Sjöström et al. (2022). During a stormier period, we expect more quartz and higher Si/Al ratios to reflect the input of coarse-grained material and increases in K-feldspar and $Cp2_{XRF}$ as indicators of mineral input (Fig. 8).

In order to assess local storm events as well as the potential storm activity information contained in each dataset, we applied changepoint modelling to each of these proxies individually. This allows us to examine the agreement between the different proxies in terms of their response to stormier periods and the noise level in a given dataset (Fig. 9). We expect stormier periods to express themselves as peaks (rather than a gradual or baseline changes) in the average weighted function where the timing of these peaks is identified using the probability distribution curves. Authors define events differently, often using the age interval from, and returning to, the baseline. With the approach used here the change is dated between the baseline and the first sample of the peak. The intervals given therefore provide conservative windows. Depending on the proxy, 5 to 9 stormier periods were identified. The fact that these four proxies, all constructed from the same sequence and using only two types of data, do not show perfectly matching storm periods demonstrates that single proxy reconstructions should be made with caution. Generally speaking, however, we can define seven local storm periods (LSP) based on the SMDS record dated to (cal yr BP): 4480–4425 (LSP-i), 3320–3190 (LSP-ii), 2150–1920 (LSP-iii), 1450 (LSP-iv), 1005–850 (LSP-v), 720–650 (LSP-vi) and 410–350 (LSP-vii).

4.5. Regional context for storm reconstruction

In order to assess and upscale our results to a more regional context, we compare the SMDS sequence with the available within-bog record SMS_{2008}, but also with regionally relevant paleostorm records including Davidsmosse and the coastal sites Hyltemossen and Undarsmosse (~60, ~100 and ~95 km southwest, respectively; Fig. 1). Changepoint modelling was also applied to each proxy individually to test coherence across the transect (Fig. 9). The SMS_{2008} study focused on trace elements acquired through acid digestion and ICP-MS/OES. With no Si data and poor analytical quality for Ti, we rely on K and Al MAR, which are both associated with mineral inputs (Kylander et al., 2013, 2016; Martinez-Cortizas et al., 2020). Potassium is hosted in K-feldspar and mica, which makes it more appropriate for comparison with the SMDS IR-inferred mineralogy, while Al is a common mineral forming element (Deer et al., 1992). The storm record from Davidsmosse is based on a multi-element PCA, where $Cp2_{XRF}$ represented the integrated behaviour of Si, Al and Ti, and Si/Al is, as mentioned previously, linked to grain size (Sjöström et al., 2022). As shown above, the input of minerals during a given change can differ slightly in timing. Elementally based approaches average the mineralogical signal because it necessarily combines the presence of all minerals hosting, in the case of SMDS and Davidsmosse, Ti, Si and Al. In contrast, the data from Hyltemossen and Undarsmosse are based on the input of particles >200 μm and maximum observed grain sizes (Björck and Clemmensen, 2004; de Jong et al., 2006). The data from the potential source sediments in this study show that, although quartz clearly dominates the coarse fraction (>63 μm), the median grain sizes are somewhat lower than 200 μm. We are therefore comparing several different types of data: IR-inferred mineralogy and minerogenic input, elementally inferred mineralogy and minerogenic input (with both ICP and XRF analytical approaches) and physical counting of grains of a slightly different size than those expected at SMDS. In addition, each record has errors associated with age modelling of the proxy data, and this can add uncertainty to the alignment of the inferred changepoints.

There is agreement between identified storm periods for the two Store Mosse records during LSP-iii (2150-1920 cal yr BP), LSP-iv (1450 cal yr BP) and LSP-vii (410-350 cal yr BP; Fig. 9). There is also overlap in timing of LSP-v (1005-850 cal yr BP) and LSP-vi (720-650 cal yr BP) with a single event in SMS_{2008} (900-700 cal yr BP). The peak in elemental MAR dated to 3000 cal yr BP at SMS_{2008} was not captured by the changepoint modelling but could be argued to be a lagged signal of LSP-ii. There are differences between SMDS and SMS_{2008} that could explain the observed pattern beyond the proxy and dating issues mentioned above. SMS_{2008} dates back to ~9 ka and by the time SMDS started accumulating peat at ~5 ka, the coring site would have been further from the bog edge. The present-day distance between the sand supply of the SMT1 dunes to SMDS is ~1 km but with the wide flat basin morphology the peat should have extended laterally fairly quickly (Fig. 1). On the other hand, SMS_{2008} is located 650 m from the present-day soil limit, which in the southern end of the bog is dominated by till and bedrock. It is 3 km to the glaciofluvial and aeolian deposits on the western edge. Thus, storm signals have to be stronger in order to carry mineral material to SMS_{2008}.

What a comparison between these two sequences may provide is an indication of shifting wind directions. Based on the morphology of the dunes at Store Mosse, there is a suggestion that at the time of deposition at ~8 to 6 ka, northwesterly winds dominated (Bjermo, 2019). This is in contrast to present day winds that are predominantly from the west (Wern and Bärring, 2009). The lack of agreement early in the record may be a function of SMDS being directly downwind (southeast) of an abundant sand source (Fig. 1). As the winds shifted to a more westerly position there was better agreement with SMS_{2008}, which is then downwind of the glaciofluvial and sand deposits to the west (albeit still at a greater distance).

For a storm signal to be generated there must be an available active sand source, strong winds and, potentially, snow cover and/or a reduction in vegetation. Already above, we see the potential impact of the distance from the sand source to the sampling site. This must also be considered at the regional level. Davidsmosse is ~30 km from the coast and from more significantly exposed sand sources but only 50–150 m away from the tills and glaciofluvial sediments that surround the bog, so there is a shorter transport distance from the mineral source than at the other sites (Sjöström et al., 2022). Hyltemossen and Undarsmosse are located 17 and 1.5 km from the coast and from a significant sand source, respectively (Fig. 9; Björck and Clemmensen, 2004; de Jong et al., 2006). Both of the coastal sites are likely more affected by human activities in the form of grazing and agriculture from 1350 to 1500 cal yr BP for Hyltemosse and Undarmosse, respectively (Björck and Clemmensen, 2004; de Jong et al., 2006). We would expect sites closer to the coast to exhibit more storm events and stronger signals and, with allowances for the different types of proxies and how storm events/periods are defined, this does not seem to be the case. The dominant wind direction of the event must also be optimal for the source-to-sink transport of the coarse-grained mineral material, which introduces site-specific variability in the records. In this, Store Mosse, which has sand deposits located to the north, south and west, may have an advantage in comparison to other sites. It is interesting to note that the events recorded inland are generally longer in duration, which may be linked to a more open landscape needed for storm signals to be generated and recorded.

When we compare records from same-core, same-site and finally, regional storm proxies, we see that there are broadly common signals. It is, however, hard to precisely define these periods in time, even just across the ~100 km transect examined here. By extension, our work shows that there is uncertainty, and thus risk, in identifying wider trends in past storminess based on single proxies or single sites. This heterogeneity problem based on proxies is consistent with historical wind observations that may yield local long-term trends at one site or for one type of storm index, while no trends are found nearby or on-site using another index (Feser et al., 2014). The differences evidenced here in proxy and site response lead to poorly defined storminess periods and thus create difficulty in linking to potential drivers, which themselves act on annual/decadal (e.g., North Atlantic Oscillation, solar activity) to millennial (e.g., orbital changes in insolation, Atlantic Meridional Overturning Circulation) timescales (Ortega et al., 2015; Steinhilber et al., 2009; Thornalley et al., 2009).

In an attempt to address these issues, we propose the building of *regional storm stacks,* which are more robust against proxy and site-specific issues. We present the Southern Sweden-Storm Stack (S Swe-StSt; Fig. 9), which is based on the changepoint structure inferred from the *joint modelling* of the paleostorm records along the studied transect (K-feldspar and $Cp2_{XRF}$ from SMDS and the elemental MAR from SMS_{2008} were excluded so that the focus was on grain-size proxies rather than more general dust signals). Joint modelling assumes that the changes in the records occur at the same time, and indeed, we expect the sites to capture the same windstorms. This approach has the advantage that the resolution of the changepoints is improved by reinforcing any common signal while reducing the influence of random noise introduced from for example, analytical uncertainties or site-specific variability. In defining regional storm periods (RSP) we considered increases in inferred functions as well as the 95% confidence interval and gave coastal sites, which should experience stronger storm signals, more weight. Peaks were seen across the majority of the proxy records for the following six RSP (cal yr BP): 4495–4290 (RSP-I), 3880–3790 (RSP-II), 2885–2855 (RSP-III), 2300–2005 (RSP-IV), 1175–1065 (RSP-V) and 715–425 (RSP-VI; Figs. 9 and 10; SD Fig. 6). The top ~300 years were excluded due to the anthropogenic impacts observed at several sites. The agreement across the sites varies, but RSP-I, -IV and -VI have the strongest cross-transect signals and the longest duration. The length of the RSP window should be considered a conservative estimate.

Given the problems of single proxy and single site reconstructions argued previously, we are constrained by the availability of paleostorm records, particularly peat based, when seeking to make comparisons. In the Scandinavian context, we find a similar broad scale storm reconstruction in Jutland in northern Denmark (i.e., directly west of the S Swe-StSt) (Clemmensen et al., 2009). Five dunefields located over ~300 km were examined for both initiation of aeolian activity and dune stabilization by soil development (Fig. 10). Initiation events were dated to 4150, 2750, 1850, 870–750 and 400-300 cal yr BP and paleosol formation to 4400, 2450, 1750 and 880 cal yr BP. Comparing dune and peat paleostorm records is not trivial since they are two very different systems. Dunes require a more significant sand source to form and sustained winds to move. In addition, optically stimulated luminescence (OSL) dating methods involve a higher degree of uncertainty than ^{14}C approaches. While the reconstruction from Denmark only dates the initiation, and not the span of, aeolian activity, what is crucial is that the periods of paleosol formation do not overlap with any of the storm periods in the S Swe-StSt. While it is beyond the scope of this article to delve deeply into the mechanisms behind Holocene storminess, Clemmensen et al. (2009) lift storm seasonality and suggest that dune activity increased during wet and cool summers caused by the southward shift of summer cyclone activity, ultimately linked to cooler high latitudes and a steeper pole-equator temperature gradient. Winters were less stormy due to frequent atmospheric blocking. Peat decomposition is reduced during such wet and cool conditions and using the SMS_{2008} decomposition proxy d_Cp1 (the detrended first component from a bulk peat FTIR analysis, this represents short term peat decomposition; Martínez-Cortizas et al., 2021b), we see at a first glance that many of the RSP, namely RSP-II, -III, -IV and -VI, overlap in time with wetter/cooler periods at Store Mosse. Particularly, RSP-II and -III match very well in time given they are such short events.

Looking at available data, there are peat paleostorm records from two sites in the Outer Hebrides (Orme et al., 2016), which can be jointly modelled with a record from the Inner Hebrides (Kylander et al., 2020), creating a longer transect of ~300 km on the western coast of Scotland. The Western Scotland-Storm Stack (W Scot-StSt, Fig. 10, SD Fig. 7) has four RSP dated to (cal yr BP): 3430–3415 (RSP-A), 2710–2570 (RSP-B), 2260–2005 (RSP-C) and 873–360 (RSP-D). When comparing with a regional study including six dune fields from Northern Ireland (Wilson et al., 2004) as well as a compilation from the Outer Hebrides (Gilbertson et al., 1999), there is reasonable overlap in activity between 4000 and 3000 cal yr BP and during the last 1000 years. Comparing both storm stacks and the proximal dune records as a whole, the only clear commonality is during the last 1000 years when an increase in storminess is registered across the board. This falls into the Little Ice

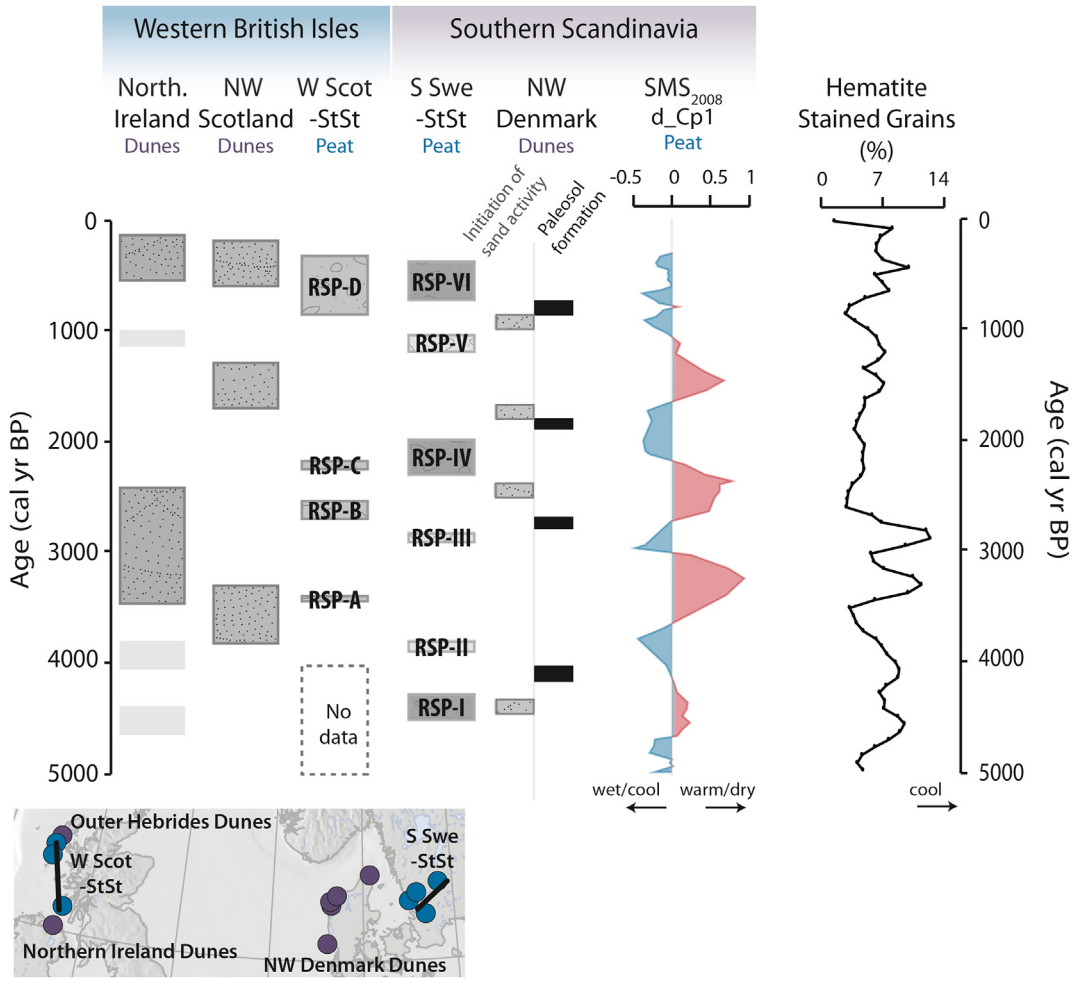

Fig. 10. Comparison of regional storm stacks with proximal records of dune activity. For the western British Isles the W Scot-StSt incorporates the signals from three records stretching across the Inner and Outer Hebrides, which are compared with dune activity from Northern Ireland and the Outer Hebrides. Crossing the North Sea, the S Swe-StSt is located to the east of a study detailing the initiation of sand activity and paleosol formation from northwestern Denmark. Increased storm periods in Scandinavia may be linked to wet and cool summers, which are indicated by low values of the peat decomposition proxy d_Cp1 (the detrended first component from an FTIR analysis of the bulk peat representing short term peat decomposition) from SMS_{2008}. Periods of cooling in the North Atlantic are reconstructed by the percentage of hematite stained grains, but these do not show a one-to-one relationship with the reconstructed RSP indicating more complex interactions. See text for references.

Age (1250–1860 Wanner et al., 2022) which is one of the few stormier periods reliably recorded in Europe across both proxies and archives (Wilson et al., 2004).

It is perhaps the differences between regional storms stacks, however, which prove to be useful in the future. Previous attempts to summarize stormier periods during the Holocene have considered much larger geographical areas and mixed different types of paleoarchives (e.g., Pouzet et al., 2018; Sorrel et al., 2012). While appropriate for some questions, this may blur spatial patterns as well as temporal resolution, particularly depending on the age uncertainties of the material used. The storm stacks presented here cover a much smaller geographic area and, given the main archive used, have better temporal resolution. This lends itself well to studying past changes in storm track position. By definition, areas within the storm track will experience stronger storminess than those at edges or outside the storm track. It cannot be expected that all sites in a broader region are equally as stormy at the same time – regional storm stacks may help tease these changes out further. For example, in looking at the period between 3000 and 2000 cal yr BP, the storm track may have moved from a more southerly position (S Swe-StSt RSP-III) to a more northerly position (W Scot-StSt RSP-B and -C) and back again (S Swe-StST RSP-IV), paralleling the variable temperature conditions in the North Atlantic as indicated by the stacked record of hematite stained grains (HSG; Bond et al., 1997). The storm track can change position in both its north-south and east-west path and a critical mass of regional storm stacks is needed to reconstruct this variability in the past.

5. Conclusions

This study develops tools for reconstructing past storminess based on FTIR-ATR analyses of the inorganic fraction of the SMDS peat sequence, which spans the last ~5000 years. Reconstructed changes in quartz, whose coarse nature was confirmed by analyses of potential source sediments found locally, were used as a proxy for wind intensity. This was further supported by Si/Al as a grain-size proxy as well as K-feldspar and $Cp2_{XRF}$ as indicators of mineral input to the bog. Changepoint modelling of these four indicators applied individually saw disparities in the timing of storm periods across the data suite and attest to differences in proxy response to the same windstorm conditions. Nonetheless, LSP could generally be dated to (cal yr BP): 4480–4425, 3320–3190, 2150–1920, 1450, 1005–850, 720–650 and 410–350. These LSP agreed fairly well with data from the SMS_{2008} sequence located

~5 km to the south, with offsets likely explained by the relative distance to mineral sources and shifting wind directions.

Comparison with regionally relevant records along a ~100 km transect showed that while records are somewhat consistent, there are differences in site response which are potentially compounded by uncertainties in age modelling of the different datasets. To address this issue, we suggest the building of regional storm stacks. Changepoint modelling of multiple datasets together allowed us to define RSP from the S Swe-StSt to 4495–4290, 3880–3790, 2885–2855, 2300–2005, 1175–1065 and 715-425 cal yr BP. Comparison with a storm stack constructed from three sites in western Scotland and proximal dune records showed a great deal of heterogeneity and may reflect the changing position of the storm track over time. The changepoint modelling approach used here does not allow for uncertainty in the age-depth models, which could lead to an effective misalignment in the changepoints between different datasets. This is a problem we plan to address in the future. We anticipate the construction of more regional storm stacks as data becomes available, with the ultimate goal of increasing our understanding of storminess drivers on centennial to millennial timescales.

Funding sources

This work was funded by grants to MEK from Vetenskapsrådet (the Swedish Research Council grant number 2019-03434), Formas (Research Council for Sustainable Development grant number 2020–01536) and the Bolin Centre for Climate Research (grant from RA5). FS received additional funding from Formas (grant number 2020–01000). Benjamin Chandler was funded by a grant from The Leverhulme Trust (MULTIPLEX; SAS-2019-075).

Author contributions

MEK conceptualised the study and the wider project with support from AMC, RB, JKS, HA and FS. Fieldwork was performed by MEK, JKS, RG, RB, HA, BTIR and BMPC. Sub-sampling and analysis were accomplished mainly by JG within the framework of her MSc project but with additional analyses by JKS and MEK. AMC did the statistical handling and interpretation of the FTIR data. KG was responsible for aspects related to the changepoint modelling. The data interpretation was done by MEK, AMC, JKS and JG. RG performed all mapping related components. HA helped with all aspects of the dune sedimentology and GPR. FS helped with all climatological theory. BTIR and BMPC were key and crucial in all GPR acquisition and data processing. MEK and AMC wrote the manuscript together with comments from all co-authors.

Declaration of competing interest

The authors declare that they have no known competing financial interests or personal relationships that could have appeared to influence the work reported in this paper.

Data availability

A link to our dataset will be made available once published.

Acknowledgements

First and foremost, we would like to express our gratitude to Carina Härlin and the rest of the staff at Store Mosse National Park for their support in the field. The county of Jönköping is thanked for providing the opportunity for us to sample in the park. We thank Mikaela Holm and Johan Ehrlén for their help during fieldwork. Austin Stout helped with the collection and analysis of the AS samples. Daniel Ellerton is gratefully acknowledged for performing the SM grain size analyses. Carina Johansson is thanked for her constant support in the lab.

Appendix A. Supplementary data

Supplementary data to this article can be found online at https://doi.org/10.1016/j.quascirev.2022.107854.

References

Ahlbrandt, T.S., 1979. Textural parameters of eolian deposits. In: McKee, E.D. (Ed.), A Study of Global Sand Seas. U.S. Geological Survey, pp. 21–52.
Alexanderson, H., 2022. Luminescence characteristics of Scandinavian quartz, their connection to bedrock provenance and influence on dating results. Quat. Geochronol. 69, 101272.
Alexanderson, H., Bernhardson, M., 2019. Late glacial and Holocene sand drift in northern Götaland and Värmland, Sweden: sediments and ages. GFF 141, 1–22. https://doi.org/10.1080/11035897.2019.1582559.
Alexanderson, H., Fabel, D., 2015. Holocene chronology of the Brattforsheden Delta and inland dune field, SW Sweden. Geochronometria 42. https://doi.org/10.1515/geochr-2015-0001.
Alexanderson, H., Murray, A.S., 2012. Problems and potential of OSL dating Weichselian and Holocene sediments in Sweden. Quat. Sci. Rev. 44, 37–50.
Álvarez-Fernández, N., Martinez-Cortizas, A., 2020. Andurinha: Make Spectroscopic Data Processing Easier. R package version 0.0.2.
Bernhardson, M., Alexanderson, H., Björck, S., Adolphi, F., 2019. Sand drift events and surface winds in south-central Sweden: from the deglaciation to the present. Quat. Sci. Rev. 209, 13–22. https://doi.org/10.1016/j.quascirev.2019.01.017.
Bjermo, T., 2019. Eoliska avlagringar och vindriktningar under holocen i och kring Store Mosse, södra Sverige. Lund University, Department of Geology. BSc Thesis.
Björck, S., Clemmensen, L.B., 2004. Aeolian sediment in raised bog deposits, Halland, SW Sweden: a new proxy record of Holocene winter storminess variation in southern Scandinavia? Holocene 14, 677–688. https://doi.org/10.1191/0959683604hl746rp.
Blaauw, M., Christen, J.A., 2011. Flexible paleoclimate age-depth models using an autoregressive gamma process. Bayesian Anal 6, 457–474. https://doi.org/10.1214/11-ba618.
Bond, G., Showers, W., Cheseby, M., Lotti, R., Almasi, P., deMenocal, P., Priore, P., Cullen, H., Hajdas, I., Bonani, G., 1997. A pervasive millennial-scale cycle in north Atlantic Holocene and glacial climates. Science 278, 1257–1266. https://doi.org/10.1126/science.278.5341.1257.
Bosch-Reig, F., Gimeno-Adelantado, J.V., Bosch-Mossi, F., Doménech-Carbó, A., 2017. Quantification of minerals from ATR-FTIR spectra with spectral interferences using the MRC method. Spectrochim. Acta A. 181, 7–12. https://doi.org/10.1016/j.saa.2017.02.012.
Bärring, L., Fortuniak, K., 2009. Multi-indices analysis of southern Scandinavian storminess 1780–2005 and links to interdecadal variations in the NW Europe–North Sea region. Int. J. Climatol. 29, 373–384. https://doi.org/10.1002/joc.1842.
Chesworth, W., Martinez-Cortizas, A., Garcıa-Rodeja, E., 2006. The redox–pH approach to the geochemistry of the Earth's land surface, with application to peatlands. In: Martini, I.P., Martinez-Cortizas, A., Chesworth, W. (Eds.), Peatlands: Evolution and Records of Environmental and Climate Changes. Elsevier Ltd., Amsterdam, pp. 175–195.
Clemmensen, L.B., Murray, A., Heinemeier, J., Jong, R. de, 2009. The evolution of Holocene coastal dunefields, Jutland, Denmark: a record of climate change over the past 5000 years. Geomorphology 105, 303–313. https://doi.org/10.1016/j.geomorph.2008.10.003.
Deer, W.A., Howie, R.A., Zussman, J., 1992. An Introduction to the Rock-Forming Minerals. Longman Scientific & Technical, Harlow.
Degen, T., Sadki, M., Bron, E., König, U., Nénert, G., 2014. The HighScore suite. Powder Diffr. 29, S13–S18. https://doi.org/10.1017/s0885715614000840.
Eller, K.B., Brenner, E., 1912. Torvdjupskarta Store Mosse Nationalpark.
Ferrat, M., Weiss, D.J., Strekopytov, S., Dong, S., Chen, H., Najorka, J., Sun, Y., Gupta, S., Tada, R., Sinha, R., 2011. Improved provenance tracing of Asian dust sources using rare earth elements and selected trace elements for palaeomonsoon studies on the eastern Tibetan Plateau. Geochem. Cosmochim. Acta 75, 6374–6399. https://doi.org/10.1016/j.gca.2011.08.025.
Feser, F., Barcikowska, M., Krueger, O., Schenk, F., Weisse, R., Xia, L., 2014. Storminess over the north Atlantic and northwestern Europe—a review. Q. J. Roy. Meteorol. Soc. 141, 350–382. https://doi.org/10.1002/qj.2364.
Gåling, J., 2019. Reconstructing Paleoclimate Changes in Northern Store Mosse: Minerals, Organic Matter and Climate. MSc thesis, Department of Geological Sciences, Stockholm University.
Gallagher, K., Bodin, T., Sambridge, M., Weiss, D., Kylander, M., Large, D., 2011. Inference of abrupt changes in noisy geochemical records using transdimensional changepoint models. Earth Planet Sci. Lett. 311, 182–194. https://doi.org/10.1016/j.epsl.2011.09.015.
Gilbertson, D.D., Schwenninger, J.-L., Kemp, R.A., Rhodes, E.J., 1999. Sand-drift and

soil formation along an exposed North Atlantic coastline: 14,000 Years of diverse geomorphological, climatic and human impacts. J. Archaeol. Sci. 26, 439–469.
Grunenwald, A., Keyser, C., Sautereau, A.M., Crubézy, E., Ludes, B., Drouet, C., 2014. Revisiting carbonate quantification in apatite (bio)minerals: a validated FTIR methodology. J. Archaeol. Sci. 49, 134–141. https://doi.org/10.1016/j.jas.2014.05.004.
Högbom, I., 1923. Ancient inland dunes of northern and Middle Europe. GFF 5, 113–243.
Högbom, I., 1913. Finiglaziale Flugsandfelder in Dalarne. GFF 35, 484–500.
Hörner, N.G., 1927. Brattforsheden – ett värmländskt randdeltekomplex och dess dyner. Geological Survey of Sweden, Stockholm.
IPCC, 2021. Climate Change 2021: the Physical Science Basis. Contribution of Working Group I to the Sixth Assessment Report of the Intergovernmental Panel on Climate Change. Cambridge University Press, Cambridge, Cambridge, United Kingdom and New York, NY, USA. https://doi.org/10.1017/9781009157896.
de Jong, R., Björck, S., Björkman, L., Clemmensen, L.B., 2006. Storminess variation during the last 6500 years as reconstructed from an ombrotrophic peat bog in Halland, southwest Sweden. J. Quat. Sci. 21, 905–919. https://doi.org/10.1002/jqs.1011.
Kaufhold, S., Hein, M., Dohrmann, R., Ufer, K., 2012. Quantification of the mineralogical composition of clays using FTIR spectroscopy. Vib. Spectrosc. 59, 29–39. https://doi.org/10.1016/j.vibspec.2011.12.012.
Kylander, M.E., Bindler, R., Cortizas, A.M., Gallagher, K., Mörth, C.-M., Rauch, S., 2013. A novel geochemical approach to paleorecords of dust deposition and effective humidity: 8500 years of peat accumulation at Store Mosse (the "Great Bog"), Sweden. Quat. Sci. Rev. 69, 69–82. https://doi.org/10.1016/j.quascirev.2013.02.010.
Kylander, M.E., Martínez-Cortizas, A., Bindler, R., Greenwood, S.L., Mörth, C.-M., Rauch, S., 2016. Potentials and problems of building detailed dust records using peat archives: an example from Store Mosse (the "Great Bog"), Sweden. Geochem. Cosmochim. Acta 190, 156–174. https://doi.org/10.1016/j.gca.2016.06.028.
Kylander, M.E., Martínez-Cortizas, A., Bindler, R., Kaal, J., Sjöström, J.K., Hansson, S.V., Silva-Sánchez, N., Greenwood, S.L., Gallagher, K., Rydberg, J., Mörth, C.-M., Rauch, S., 2018. Mineral dust as a driver of carbon accumulation in northern latitudes. Sci. Rep. 8, 6876. https://doi.org/10.1038/s41598-018-25162-9.
Kylander, M.E., Söderlindh, J., Schenk, F., Gyllencreutz, R., Rydberg, J., Bindler, R., Cortizas, A.M., Skelton, A., 2020. It's in your glass: a history of sea level and storminess from the Laphroaig Bog, Islay (southwestern Scotland). Boreas 49, 152–167. https://doi.org/10.1111/bor.12409.
Lageräs, P., 1996. Farming and forest dynamics in an agriculturally marginal area of southern Sweden, 5000 BC to present: a palynological study of Lake Avegöl in the Småland Uplands. Holocene 6, 301–314.
Lawrence, C.R., Neff, J.C., 2009. The contemporary physical and chemical flux of aeolian dust: a synthesis of direct measurements of dust deposition. Chem. Geol. 267, 46–63. https://doi.org/10.1016/j.chemgeo.2009.02.005.
Loisel, J., Yu, Z., Beilman, D.W., Camill, P., Alm, J., et al., 2014. A database and synthesis of northern peatland soil properties and Holocene carbon and nitrogen accumulation. Holocene 24, 1028–1042. https://doi.org/10.1177/0959683614538073.
Longman, J., Veres, D., Ersek, V., Salzmann, U., Hubay, K., Bormann, M., Wennrich, V., Schäbitz, F., 2017. Periodic input of dust over the Eastern Carpathians during the Holocene linked with Saharan desertification and human impact. Clim. Past 13, 897–917. https://doi.org/10.5194/cp-13-897-2017.
Lundqvist, J., Wohlfarth, B., 2000. Timing and east–west correlation of south Swedish ice marginal lines during the Late Weichselian. Quat. Sci. Rev. 20, 1127–1148. https://doi.org/10.1016/s0277-3791(00)00142-6.
Martinez-Cortizas, A., López-Costas, O., Orme, L., Mighall, T., Kylander, M.E., Bindler, R., Gallego-Sala, A., 2020. Holocene atmospheric dust deposition in NW Spain. Holocene 30, 507–518. https://doi.org/10.1177/0959683619875193.
Martínez-Cortizas, A., López-Merino, L., Silva-Sánchez, N., Sjöström, J.K., Kylander, M.E., 2021a. Investigating the mineral composition of peat by combining FTIR-ATR and multivariate analysis. Minerals 11, 1084. https://doi.org/10.3390/min11101084.
Martínez-Cortizas, A., Sjöström, J.K., Ryberg, E.E., Kylander, M.E., Kaal, J., López-Costas, O., Fernández, N.Á., Bindler, R., 2021b. 9000 years of changes in peat organic matter composition in Store Mosse (Sweden) traced using FTIR-ATR. Boreas 50, 1161–1178. https://doi.org/10.1111/bor.12527.
Müller, C.M., Pejcic, B., Esteban, L., Piane, C.D., Raven, M., Mizaikoff, B., 2014. Infrared attenuated total reflectance spectroscopy: an innovative strategy for analyzing mineral components in energy relevant systems. Sci. Rep. 4, 6764. https://doi.org/10.1038/srep06764.
Mycielska-Dowgiałło, E., 1993. Estimates of late glacial and Holocene aeolian activity in Belgium, Poland and Sweden. Boreas 22, 165–170.
Orme, L.C., Davies, S.J., Duller, G.A.T., 2015. Reconstructed centennial variability of late Holocene storminess from Cors Fochno, Wales, UK. J. Quat. Sci. 30, 478–488. https://doi.org/10.1002/jqs.2792.
Orme, L.C., Reinhardt, L., Jones, R.T., Charman, D.J., Barkwith, A., Ellis, M.A., 2016. Aeolian sediment reconstructions from the Scottish Outer Hebrides: late Holocene storminess and the role of the North Atlantic Oscillation. Quat. Sci. Rev. 132, 15–25. https://doi.org/10.1016/j.quascirev.2015.10.045.
Ortega, P., Lehner, F., Swingedouw, D., Masson-Delmotte, V., Raible, C.C., Casado, M., Yiou, P., 2015. A model-tested North Atlantic Oscillation reconstruction for the past millennium. Nature 523, 71–74. https://doi.org/10.1038/nature14518.
Panait, A.M., Hutchinson, S.M., Diaconu, A.-C., Tanţău, I., Feurdean, A., 2019. Disentangling dust and sand deposition using a peat record in CE Europe (northern Romania): a multiproxy approach. Palaeogeogr. Palaeoclimatol. Palaeoecol. 532, 109257. https://doi.org/10.1016/j.palaeo.2019.109257.
Pouzet, P., Maanan, M., Piotrowska, N., Baltzer, A., Stéphan, P., Robin, M., 2018. Chronology of Holocene storm events along the European Atlantic coast. Prog. Phys. Geogr. Earth. Environ. 42, 431–450. https://doi.org/10.1177/0309133318776500.
Pratte, S., Bao, K., Sapkota, A., Zhang, W., Shen, J., Roux, G.L., Vleeschouwer, F.D., 2019. 14 kyr of atmospheric mineral dust deposition in north-eastern China: a record of palaeoclimatic and palaeoenvironmental changes in the Chinese dust source regions. Holocene 30, 492–506. https://doi.org/10.1177/0959683619892661.
Pye, K., Tsoar, H., 2009. Aeolian Sand and Sand Dunes. Springer, Berlin, Heidelberg. https://doi.org/10.1007/978-3-540-85910-9.
Reimer, P.J., Reimer, P.J., et al., 2020. The IntCal20 northern hemisphere radiocarbon age calibration curve (0–55 cal kBP). Radiocarbon 62, 725–757. https://doi.org/10.1017/rdc.2020.41, 2020.
Reynolds, J.M., 2011. An Introduction to Applied and Environmental Geophysics, second ed. Wiley, Chichester.
Rietveld, 1969. A profile refinement method for nuclear and magnetic structures. J. Appl. Crystallogr. 2. https://doi.org/10.1107/s0021889869006558.
Rudmin, M., Ruban, A., Savichev, O., Mazurov, A., Dauletova, A., Savinova, O., 2018. Authigenic and detrital minerals in peat environment of vasyugan Swamp, western Siberia. Minerals 8, 500. https://doi.org/10.3390/min8110500.
Rutgersson, A., Jaagus, J., Schenk, F., Stendel, M., 2014. Observed changes and variability of atmospheric parameters in the Baltic Sea region during the last 200 years. Clim. Res. 61, 177–190. https://doi.org/10.3354/cr01244.
Rutgersson, A., Kjellström, E., Haapala, J., Stendel, M., Danilovich, I., Drews, M., Jylhä, K., Kujala, P., Larsén, X.G., Halsnæs, K., Lehtonen, I., Luomaranta, A., Nilsson, E., Olssom, T., Särkkä, J., Tuomi, L., Wasmund, N., 2022. Natural hazards and extreme events in the Baltic Sea region. Earth Sys. Dyn. 13, 251–301. https://doi.org/10.5194/esd-13-251-2022.
Ryberg, E.E., Väliranta, M., Martinez-Cortizas, A., Ehrlén, J., Sjöström, J.K., Kylander, M.E., 2022. Postglacial peatland vegetation succession in Store Mosse bog, south-central Sweden: an exploration of factors driving species change. Boreas 51, 651–666. https://doi.org/10.1111/bor.12580.
Schenk, F., Zorita, E., 2012. Reconstruction of high resolution atmospheric fields for Northern Europe using analog-upscaling. Clim. Past 8, 1681–1703. https://doi.org/10.5194/cp-8-1681-2012.
SGU, 2022a. Bedrock 1:1 000 000 © Sveriges Geologiska Undersökning.
SGU, 2022b. Quaternary Map 1:25 000 - 1:100 000 © Sveriges Geologiska Undersökning.
SGU, 2021. Glacial Striations Map 1:500000 © Sveriges Geologiska Undersökning.
Shotyk, W., Weiss, D., Kramers, J.D., Frei, R., Cheburkin, A.K., Gloor, M., Reese, S., 2001. Geochemistry of the peat bog at Etang de la Gruère, Jura Mountains, Switzerland, and its record of atmospheric Pb and lithogenic trace metals (Sc, Ti, Y, Zr, and REE) since 12,370 14C yr BP. Geochem. Cosmochim. Acta 65, 2337–2360. https://doi.org/10.1016/s0016-7037(01)00586-5.
Sjögren, P., 2009. Sand mass accumulation rate as a proxy for wind regimes in the SW Barents Sea during the past 3 ka. Holocene 19, 591–598. https://doi.org/10.1177/0959683609104033.
Sjöström, J.K., Bindler, R., Cortizas, A.M., Björck, S., Hansson, S.V., Karlsson, A., Ellerton, D.T., Kylander, M.E., 2022. Late Holocene peat paleodust deposition in south-western Sweden - exploring geochemical properties, local mineral sources and regional aeolian activity. Chem. Geol. 602, 120881. https://doi.org/10.1016/j.chemgeo.2022.120881.
Sjöström, J.K., Bindler, R., Granberg, T., Kylander, M.E., 2019. Procedure for organic matter removal from peat samples for XRD mineral analysis. Wetlands 39, 473–481. https://doi.org/10.1007/s13157-018-1093-7.
Sjöström, J.K., Cortizas, A.M., Hansson, S.V., Sánchez, N.S., Bindler, R., Rydberg, J., Mörth, C.-M., Ryberg, E.E., Kylander, M.E., 2020. Paleodust deposition and peat accumulation rates – bog size matters. Chem. Geol. 554, 119795. https://doi.org/10.1016/j.chemgeo.2020.119795.
Skogsstyrelsen, 2017. Efter Gudrun: Erfarenheter Av Stormen Och Rekommendationer for Framtiden.
SMHI, 2022. Wind Direction and Wind Speed: SMHI Station Network accessed 2022-10-11.
SMHI, 2015. Skogsskador Efter Gudrun [WWW Document]. URL accessed 2022-2-9.
SMHI, 2009. Average Measured Yearly Precipitation, pp. 1961–1990 [WWW Document]. URL accessed 2022-2-9.
SMHI, 2005. Gudrun - Januaristormen 2005 [WWW Document]. URL accessed 2022-10-12.
Sohlenius, G., Lax, K., Ladenberger, A., 2009. Kan SGUs Data Användas För Att Uppskatta Moränens Transportlängd? Sveriges geologiska undersökning. Report No. 2009:26.
Sorrel, P., Debret, M., Billeaud, I., Jaccard, S.L., McManus, J.F., Tessier, B., 2012. Persistent non-solar forcing of Holocene storm dynamics in coastal sedimentary archives. Nat. Geosci. 5, 892–896. https://doi.org/10.1038/ngeo1619.
Steinhilber, F., Beer, J., Fröhlich, C., 2009. Total solar irradiance during the Holocene. Geophys. Res. Lett. 36. https://doi.org/10.1029/2009gl040142.
Stendel, M., , Beddeslaar, E.J.M.V. den, Hannachi, A., Kent, E., Lefebvre, C., Schenk, F., Schrier, G., Woolings, T., 2016. Recent change - atmosphere. In: Quante, M.,

Colijn, F. (Eds.), North Sea Region Climate Change Assessment. Springer, Cham, pp. 55–84.
Stevens, T., Sechi, D., Tziavaras, C., Schneider, R., Banak, A., Andreucci, S., Hättestrand, M., Pascucci, V., 2022. Age, formation and significance of loess deposits in central Sweden. Earth. Surf. Process. 1–26. https://doi.org/10.1002/esp.5456.
Stewart, H., Bradwell, T., Bullard, J., Davies, S.J., Golledge, N., McCulloch, R.D., 2017. 8000 years of North Atlantic storminess reconstructed from a Scottish peat record: implications for Holocene atmospheric circulation patterns in Western Europe. J. Quat. Sci. 32, 1075–1084. https://doi.org/10.1002/jqs.2983.
Svensson, G., 1988. Bog development and environmental conditions as shown by the stratigraphy of Store Mosse mire in southern Sweden. Boreas 17, 89–111. https://doi.org/10.1111/j.1502-3885.1988.tb00126.x.
Tegen, I., Fung, I., 1994. Modeling of mineral dust in the atmosphere: sources, transport, and optical thickness. J. Geophys. Res. 99, 22 897–922 914.
Thornalley, D.J.R., Elderfield, H., McCave, I.N., 2009. Holocene oscillations in temperature and salinity of the surface subpolar North Atlantic. Nature 457, 711–714. https://doi.org/10.1038/nature07717.
Toby, B.H., 2006. Rietveld analysis: how good is good enough? Powder Defrac 21, 67–79. https://doi.org/10.1154/1.2179804.
Vassilev, S.V., Baxter, D., Andersen, L.K., Vassileva, C.G., Morgan, T.J., 2012. An overview of the organic and inorganic phase composition of biomass. Fuel 94, 1–33. https://doi.org/10.1016/j.fuel.2011.09.030.
Wanner, H., Pfister, C., Neukom, R., 2022. The variable European little ice age. Quat. Sci. Rev. 287, 107531. https://doi.org/10.1016/j.quascirev.2022.107531.
Watts, H., Booth, A.D., Reinardy, B.T.I., Killingbeck, S.F., Jansson, P., Clark, R.A., Chandler, B., Nesje, A., 2022. An assessment of geophysical survey techniques for characterising the subsurface around glacier Margins, and recommendations for future applications. Front. Earth Sci. 10, 734682. https://doi.org/10.3389/feart.2022.734682.
Wedepohl, K.H., 1995. The composition of the continental crust. Geochem. Cosmochim. Acta 59, 1217–1232. https://doi.org/10.1016/0016-7037(95)00038-2.
Weiss, D., Shotyk, W., Rieley, J., Page, S., Gloor, M., Reese, S., Martinez-Cortizas, A., 2002. The geochemistry of major and selected trace elements in a forested peat bog, Kalimantan, SE Asia, and its implications for past atmospheric dust deposition. Geochem. Cosmochim. Acta 66, 2307–2323. https://doi.org/10.1016/s0016-7037(02)00834-7.
Wern, L., Bärring, L., 2009. Sveriges Vindklimat 1901-2008: Analys Av Trend I Geostrofisk Vind. SMHI.
Wilson, P., McGourty, J., Bateman, M.D., 2004. Mid-to late-Holocene coastal dune event stratigraphy for the north coast of Northern Ireland. Holocene 14, 406–416. https://doi.org/10.1191/0959683604hl716rp.